

Final Report to the AIR FORCE OFFICE OF SCIENTIFIC RESEARCH

AFOSR Grant FA9550-04-1-0386, Period: 06-01-2004 to 12-31-2005

AERO-OPTICAL WAVEFRONT PROPAGATION AND REFRACTIVE FLUID INTERFACES
IN LARGE-REYNOLDS-NUMBER COMPRESSIBLE TURBULENT FLOWS

Principal Investigator: Prof. Haris J. Catrakis, University of California, Irvine

Program Manager: Lt. Col. Dr. Rhett Jefferies, Unsteady and Rotating Flows Program

Abstract

The physical behavior of refractive fluid interfaces in turbulent compressible separated shear layers and the resulting structure of the aero-optical wavefronts have been investigated using new experimental studies and physical modeling. The experiments utilize the new AFOSR/UCI variable-pressure facility which generates large Reynolds number flows with elevated pressures in the test section crucial for direct imaging of the refractive field and interfaces. Direct, non-intrusive, and non-integrated imaging of the refractive index field in purely gaseous flows is achieved using laser induced fluorescence of acetone vapor molecularly premixed in air and recorded with a high-resolution intensified digital camera system, simultaneously with profiles of the propagated laser wavefronts recorded with a high-resolution Shack-Hartmann sensor. Three key accomplishments have been made. Firstly, direct examination of the aero-optical interactions at every location along the laser propagation path in the flow has been achieved. Secondly, a new aero-optical interaction mechanism has been discovered in which non-monotonic behavior of the cumulative aero-optical aberrations can occur depending on the location of the dominant refractive interfaces. Thirdly, significant resolution robustness has been observed for the effects of the refractive field on the laser aberrations. These three accomplishments are aimed toward the development of new directed energy capabilities for airborne vehicles.

1. Outline of Publications, Presentations, Personnel, and AFRL/Industrial Interactions During Grant Period

Journal Publications:

The following journal papers have been published on the basis of the work conducted during this grant, including follow-up results from two previous grants (F49620-02-1-0142 and F49620-02-1-0277) that have been published during this grant period:

2006 “*Large Scale Refractive Turbulent Interfaces and Aero-Optical Interactions in High Reynolds Number Compressible Separated Shear Layers*,” Catrakis, H. J., Aguirre, R. C., Nathman, J. C., & Garcia, P. J., *Journal of Turbulence*, Accepted for Publication and in Press.

2005 “*Experimental Studies of Turbulent Interfaces in Mixing, Aero-Optics, and High-*

Report Documentation Page			Form Approved OMB No. 0704-0188		
Public reporting burden for the collection of information is estimated to average 1 hour per response, including the time for reviewing instructions, searching existing data sources, gathering and maintaining the data needed, and completing and reviewing the collection of information. Send comments regarding this burden estimate or any other aspect of this collection of information, including suggestions for reducing this burden, to Washington Headquarters Services, Directorate for Information Operations and Reports, 1215 Jefferson Davis Highway, Suite 1204, Arlington VA 22202-4302. Respondents should be aware that notwithstanding any other provision of law, no person shall be subject to a penalty for failing to comply with a collection of information if it does not display a currently valid OMB control number.					
1. REPORT DATE 31 MAR 2006		2. REPORT TYPE N/A		3. DATES COVERED -	
4. TITLE AND SUBTITLE Aero-Optical Wavefront Propagation and Refractive Fluid Interfaces in Large-Reynolds-Number Compressible Turbulent Flows				5a. CONTRACT NUMBER	
				5b. GRANT NUMBER	
				5c. PROGRAM ELEMENT NUMBER	
6. AUTHOR(S)				5d. PROJECT NUMBER	
				5e. TASK NUMBER	
				5f. WORK UNIT NUMBER	
7. PERFORMING ORGANIZATION NAME(S) AND ADDRESS(ES) Prof. Haris J. Catrakis, Principal Investigator Mechanical and Aerospace Engineering University of California, Irvine 4200 Engineering Gateway Irvine, CA 92697-3975				8. PERFORMING ORGANIZATION REPORT NUMBER	
9. SPONSORING/MONITORING AGENCY NAME(S) AND ADDRESS(ES)				10. SPONSOR/MONITOR'S ACRONYM(S)	
				11. SPONSOR/MONITOR'S REPORT NUMBER(S) AFRL-SR-AR-TR06-0229	
12. DISTRIBUTION/AVAILABILITY STATEMENT Approved for public release, distribution unlimited					
13. SUPPLEMENTARY NOTES The original document contains color images.					
14. ABSTRACT					
15. SUBJECT TERMS					
16. SECURITY CLASSIFICATION OF:			17. LIMITATION OF ABSTRACT SAR	18. NUMBER OF PAGES 44	19a. NAME OF RESPONSIBLE PERSON
a. REPORT unclassified	b. ABSTRACT unclassified	c. THIS PAGE unclassified			

Speed Flows,” Aguirre, R. C., Mason, J. O., & Catrakis, H. J., World Scientific and Engineering Academy and Society: Transactions on Mechanical Engineering, Vol. 2, No. 1, pp. 50-58.

- 2005 “*Computational Aero-Optics and Electromagnetics: Compressible Vortices and Laser Beam Propagation,*” Aguirre, R. C., Mason, J. O., & Catrakis, H. J., *World Scientific and Engineering Academy and Society: Transactions on Mechanical Engineering*, Vol. 2, No. 1, pp. 19-27.
- 2005 “*Physical Modeling of Turbulent Fluid Interfaces and Flow Regions at Large Reynolds Numbers,*” Catrakis, H. J., Aguirre, R. C., & Mason, J. O., *World Scientific and Engineering Academy and Society: Transactions on Mechanical Engineering*, Vol. 2, No. 1, pp. 1-19.
- 2004 “*Aero-Optical Wavefronts and Scale-Local Characterization in Large Reynolds Number Compressible Turbulence,*” Aguirre, R. C. & Catrakis, H. J., *American Institute of Aeronautics and Astronautics Journal*, Vol. 42, No. 10, pp. 1982-1990.
- 2004 “*New Interfacial Fluid Thickness Approach in Aero-Optics with Applications to Compressible Turbulence,*” Catrakis, H. J. & Aguirre, R. C., *American Institute of Aeronautics and Astronautics Journal*, Vol. 42, No. 10, pp. 1973-1981.

Conference Presentations and Papers:

The following conference presentations and papers on the aero-optics research conducted in this grant period have been presented at national conferences of the AIAA (American Institute of Aeronautics and Astronautics), DEPS (Directed Energy Professional Society), SPIE (Society of Photo-Instrumentation Engineers, now known as International Society for Optical Engineering), and TSFP (Turbulence and Shear Flow Phenomena) as follows:

- 2005 “*Aero-Optical Two-Way Interactions and High Energy Laser Beam Propagation in Large Reynolds Number Turbulence,*” Catrakis, H. J., Garcia, P. J., Nathman, J. C., & Zubair, F. R. 8th Annual Directed Energy Symposium, Directed Energy Professional Society (DEPS), High Energy Laser Beam Control and Optics II Session, Lihue, Kauai, Hawaii.
- 2005 “*Direct Examination of Turbulent Refractive Index Variations Along Laser Beam Propagation Paths and Corresponding Optical-Wavefront Distortions,*” Aguirre, R. C., Nathman, J. C., Garcia, P. J., & Catrakis, H. J., *Free-Space Laser Communications V, International Society for Optical Engineering (SPIE), San Diego, CA, Paper 5892-21.*
- 2005 “*Turbulent Fluid Interfaces and Regions in Aero-Optics and Mixing,*” Catrakis, H. J., Aguirre, R. C., Nathman, J. C., & Garcia, P. J., 4th International Symposium on Turbulence & Shear Flow Phenomena (TSFP4), Williamsburg, VA, Paper TSFP4-217.

- 2005 *“Imaging of Turbulent Refractive Interfaces and Optical Wavefronts in Aero-Optics,”* Aguirre, R. C., Nathman, J. C., Garcia, P. J., & Catrakis, H. J., 36th AIAA Plasmadynamics & Lasers Conference, Toronto, CA, AIAA Paper 2005-4656.
- 2005 *“Turbulent Refractive Fluid Interfaces and Aero-Optical Wavefront Distortions: Experiments and Computations,”* Aguirre, R. C., Nathman, J. C., Garcia, P. J., & Catrakis, H. J., 43rd AIAA Aerospace Sciences Meeting and Exhibit, Reno, NV, AIAA Paper 2005-1080.
- 2004 *“Large-Reynolds-Number Compressible Separated Shear Layers: Aero-Optical Interactions and Control,”* Aguirre, R. C., Nathman, J. C., & Catrakis, H. J., 35th AIAA Plasmadynamics & Lasers Conference, Portland, OR, AIAA Paper 2004-2442.
- 2004 *“Aero-Optical Interactions in Turbulent Compressible Separated Shear Layers and the Interfacial Fluid Thickness Approach,”* Aguirre, R. C., Nathman, J. C., & Catrakis, H. J., 42nd AIAA Aerospace Sciences Meeting and Exhibit, Reno, NV, AIAA Paper 2004-0473.

Personnel Conducting Research:

The research during this grant period has been conducted by the PI and several Ph.D./M.S. graduate students as follows:

Catrakis, Haris J.	Associate Professor, University of California, Irvine
Aguirre, Roberto C.	Graduated with Ph.D. in June 2005, UC Irvine
Nathman, Jennifer C.	Graduated with M.S. in November 2005, UC Irvine
Garcia, Philip, J.	Ph.D./M.S. Graduate Student, UC Irvine
Zubair, Fazlul R.	Ph.D./M.S. Graduate Student, UC Irvine

AFRL Interactions and Industrial Interactions:

The PI maintains contact with the following members of the Directed Energy (DE) Directorate at AFRL, Kirtland AFB, in Albuquerque, NM:

Martinez, Rudy	Senior Scientist & DE Strategic Planner
Schlie, Vern	Senior Scientist, Laser Technology

The AFRL interactions focus on basic high-energy laser and low-energy laser aspects of aero-optical interactions for high-speed and high-maneuverability aircraft, such as tactical fighter aircraft, for the development of hardware such as novel laser turret designs with flow/beam control as well as software such as computational simulation codes and airborne directed-energy simulators.

Industrially, the PI maintains contact with Dr. Michael Jones of Lockheed Martin (Ft. Worth, TX) regarding airborne directed-energy aspects and Dr. James Trolinger of MetroLaser (Irvine, CA) regarding remote laser imaging of turbulence properties for airborne directed-energy systems.

2. Description of Major Research Accomplishments

In aero-optics, as discussed in review articles [1, 2], one of the basic goals is to relate physically the behavior of turbulence-generated refractive index fields to the structure of turbulence-distorted optical wavefronts. Ever since some of the earliest studies in the field of aero-optics [3, 4], advances in both the understanding of turbulence and its relation to the optical behavior have been sought theoretically, experimentally, and computationally (e.g. [5, 6, 7, 8, 9, 10]). Knowledge of the aero-optical interactions, identification of the dominant flow mechanisms in the generation of the aero-optical distortions, and optimization of the aero-optical interactions by using flow control where possible and optical control, are needed in both basic and applied problems in aero-optics especially where laser beam propagation needs to be utilized [1]. Improved knowledge of laser interactions in turbulent flows is useful for a variety of fundamental and technological problems ranging from basic methods for probing the behavior of large Reynolds number flows in the laboratory, in the field, and for remote sensing [11, 12, 13], to practical techniques for beam propagation from directed energy systems on airborne vehicles [1, 7, 10, 14], for example. At large Reynolds numbers, the flow structure and resulting laser beam behavior are accessible at present only through experiments either in the laboratory or in the field. Furthermore, one can appreciate that knowledge of the propagated beam behavior only, or of the integrated flow behavior only, does not uniquely relate to the aero-optical interactions. This is because the optical aberrations resulting from refractive-index variations integrate the flow structure along the beam propagation path. Thus one needs a means to enable the examination of the aero-optical interactions at each location along the beam path.

With regard to refractive turbulent fields, the basic physical interactions between the propagating optical wavefronts and the aberrating turbulent flows occur across the refractive fluid interfaces [10]. Thus, an improved understanding of the turbulent interfacial behavior is needed [15, 16, 17, 2, 18]. At large Reynolds numbers, however, turbulent refractive interfaces are highly irregular and span a wide range of scales. Thus, experimental studies at large Reynolds numbers are particularly desirable as a means to complement computational studies and physical modeling. This is because direct numerical simulations are at present limited to moderate Reynolds numbers [19] and large-eddy simulations can be sensitive to sub-grid scale modeling [20, 8]. Furthermore, depending on the problem of interest, one would like also to incorporate compressibility effects and flow geometry effects on the modeling of the large Reynolds number behavior. Previous work in aero-optics includes studies of both the large scale properties [21, 6, 9, 10] and small scale properties [22, 23, 8]. The available studies indicate that the near field aero-optical effects, in turbulent shear flows, are dominated by the large scale flow structures (e.g. [9, 10]). In addition, knowledge of the large scale aero-optical behavior can be expected to be useful regarding modeling of the cumulative contributions of the small scales, relative to the large scales, for various Air Force applications involving directed energy propagation.

In the research conducted in this grant period, a key focus is on the role of refractive interfaces in the large scale aero-optical interactions in high Reynolds number separated compressible shear layers. For this purpose, the new variable pressure flow facility at

UC Irvine developed by the PI with prior AFOSR/DURIP support (F49620-02-1-0277) is utilized to generate the separated shear layers. The freestream consists of air seeded with acetone vapor and the ambient gas is air. The flow imaging technique consists of direct imaging of the refractive index field and interfaces using laser induced fluorescence and digital photography techniques. An ultraviolet laser sheet excites the acetone vapor fluorescence which is in the visible spectrum and is recorded with a digital camera system. This enables recording of two-dimensional spatial images of the refractive index field. The Reynolds number based on the visual thickness is $Re \sim 6 \times 10^6$ and the convective Mach number is $M_c \sim 0.4$. The refractive index fields are analyzed to identify the refractive interfaces. Complex networks of spatially isolated high gradient boundaries are evident both in the interior of the flow and in the outer regions. Examination of the data shows that these high gradient boundaries contain crucial information regarding the production of large scale aero-optical aberrations. The extent to which the aero-optical aberrations depend on reduction in refractive field information is also investigated in the context of physical modeling based on the high gradient interfaces.

The aero-optics variable pressure flow facility utilized in the present investigations is shown in figure 1. The facility permits experiments at elevated test section pressures, in the range $1 \lesssim p \lesssim 20$ atm, in order to enable higher signal-to-noise ratio flow imaging than would be possible at atmospheric or sub-atmospheric pressures. For imaging techniques based on laser induced fluorescence, such as the method presently used, the resulting image signal-to-noise ratio is greater due to the increased local density of air molecules as a result of the higher operating pressures.

The laboratory facility primarily consists of a blow-down wind tunnel contained inside a variable pressure vessel. The main aero-optics vessel, in which the tunnel is housed, is oriented vertically and is shown on the right part of figure 1. The gas reservoir, which supplies fluid to the tunnel, is oriented horizontally and is shown in the left part of figure 1. The reservoir is rated at a maximum supply pressure of $\sim 3,000$ psi or ~ 200 atm. The aero-optics vessel that houses the test section is rated at a maximum operating pressure of ~ 300 psi or ~ 20 atm. The main vessel is eight feet in height and four feet in diameter, enabling two persons to stand upright in the interior when reconfiguring the tunnel and its test section. The main vessel has a quick-release entrance door of two feet in diameter that facilitates access in and out of the vessel in order to reconfigure as necessary the blow-down wind tunnel and its test section contained in the interior of the vessel. Both the main pressure vessel and the reservoir vessel are “U”-stamp ASME rated. Two ellipsoidal cap sections, for each vessel, are welded at the two ends of the main cylindrical sections. Both vessels including the quick-release door mechanism were fabricated by Melco Steel. The main vessel and the reservoir vessel are equipped with NPT fittings for attachments of vacuum lines, pressure gauges and transducers, and other instrumentation necessary for flow management.

Extensive optical access to the interior of the main pressure vessel is available through five high optical quality spectrosil windows each of 10-in. diameter and 3.25-in. thickness. Four of the five windows are vertical optical ports on the four sides of the vessel. The fifth window is a horizontal optical port on the top of the vessel. Combined with laser diagnostics, as shown in figure 2, the facility is capable of quantitative high resolution



Figure 1: Photograph of the aero-optics variable pressure flow facility at UC Irvine developed by the PI with prior AFOSR/DURIP support. The main pressure vessel is visible in the right part of the photograph. It has a large interior and cross section, extensive optical access, and a quick release door, to facilitate investigations of aero-optical phenomena at variable pressures. Combined with laser and imaging diagnostics, this facility enables high resolution flow imaging and beam measurements of aero-optical flows at large Reynolds numbers with compressibility effects. The blow-down wind tunnel and test section are housed inside the main vessel.

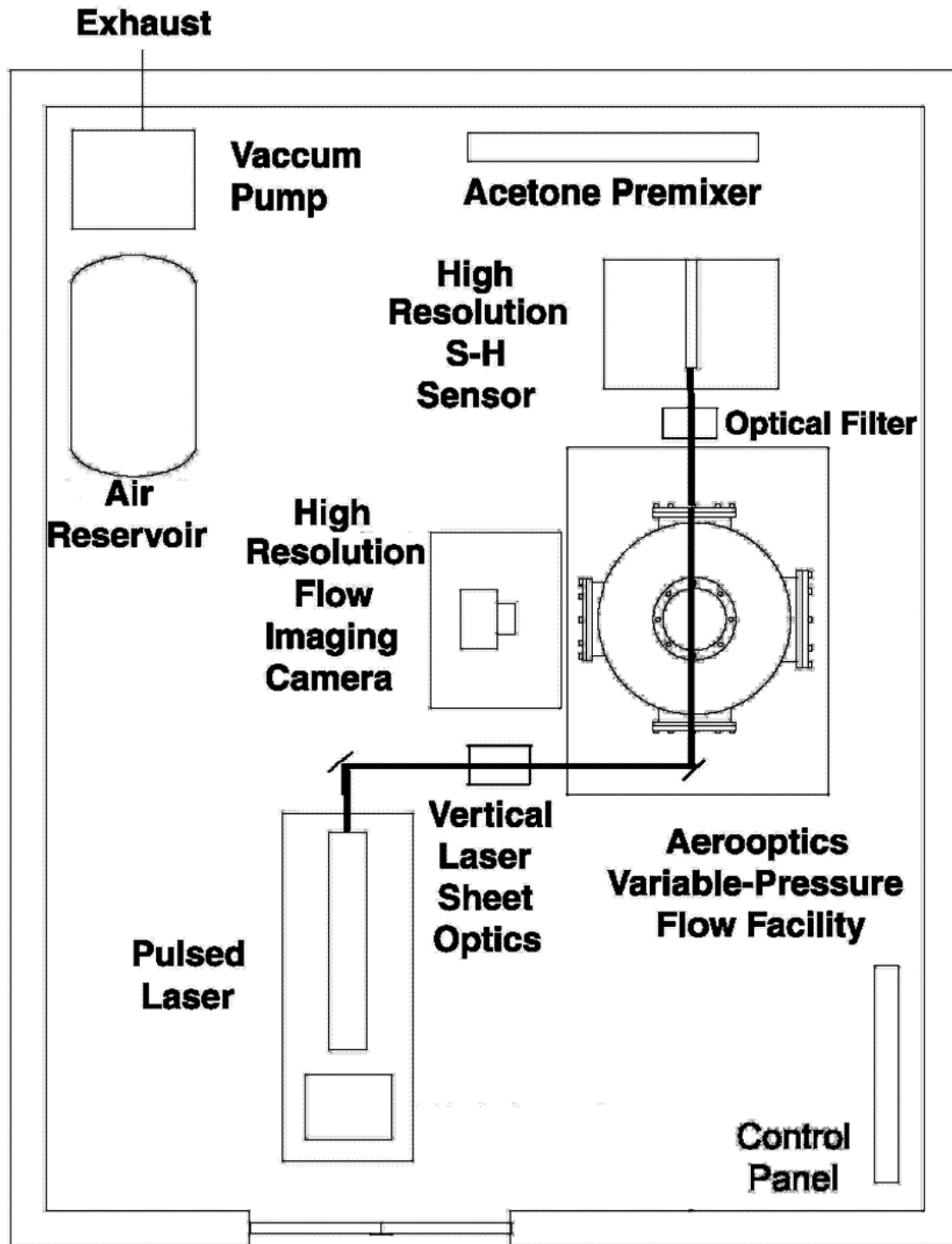


Figure 2: Schematic of the laser illumination and flow imaging configuration. A pulsed ultraviolet laser beam is shaped into a parallel laser sheet, by utilizing a parabolic mirror, and is propagated through the quartz windows of the pressure vessel and into the test section, cf. figure 1. A high resolution digital intensified charge coupled device (CCD) camera captures the visible fluorescence from the acetone vapor that is molecularly seeded in air. The laser sheet propagation direction and the flow imaging direction are mutually orthogonal.

imaging of compressible turbulent flows at large Reynolds numbers.

The flow geometry presently examined is the separated turbulent shear layer which is an example of a separated flow relevant in a wide range of applications in aero-optics (e.g. [5]). A schematic of the flow geometry is shown in figure 3. In the actual experiments, the flow is directed vertically upward and the laser propagation is horizontal, cf. figure 2. The separated shear layer represents a basic flow configuration of interest for future studies of more complex flow geometries. For example, while separated flows over curved surfaces have an unsteady separation point, the sharp 90° corner of the present flow geometry ensures a fixed separation point. Studies of the unforced separated shear layer can provide useful baseline information to evaluate the extent to which active flow control techniques such as large scale disorganization or regularization can be effective (e.g. [14, 1]).

In contrast to two-stream shear layers which typically have smaller growth rates (e.g. [24]), the separated shear layer or single-stream shear layer has a relatively large growth rate. A large growth rate is desirable in laboratory studies because it facilitates higher resolution flow imaging due to the large flow scales. While this is preferable for fundamental studies such as the present ones, one needs to keep in mind that in practical aero-optical systems a reduction in the growth rate is generally desirable since that would limit the extent of the aberrating flow field. It is essential to appreciate that the separated shear layer, as indicated in figure 3, does not exhibit reattachment as long as the perpendicular wall around the separation point extends sufficiently to ensure ample entrainment of the ambient fluid [25]. This is in contrast to flows over backward-facing steps, of finite step height, which exhibit re-attachment.

In the present experiments, the elevated test section pressure ($p \sim 3 \text{ atm}$) and the relatively large size of the vessel have resulted in a Reynolds number of:

$$Re \sim 6 \times 10^6, \quad (1)$$

based on the visual thickness $L \sim 0.1 \text{ m}$ of the shear layer in the far field, where the laser induced fluorescence imaging is conducted, and on the freestream velocity which is $U \sim 300 \text{ m/sec}$ for a convective Mach number of $M_c \sim 0.4$. The high Reynolds number achieved corresponds to flow conditions well above the mixing transition, i.e. the change in mixing behavior and specifically the pronounced increase in the mixed fluid fraction that is directly associated with the transition to fully developed turbulence, which requires at least $Re \sim 10^4$ [26].

Figure 4 shows examples of flow shadowgraphs at convective Mach numbers of $M_c \sim 0$, $M_c \sim 0.2$, and $M_c \sim 0.4$, with increasing compressibility corresponding to the images shown from top to bottom in the figure. The shadowgraphs were recorded in the present studies by collimating 10-inch diameter beams with a parabolic mirror and propagating the beams in a spanwise direction normal to the shear layers. The test section pressure for the present studies is:

$$p \sim 3 \text{ atm}. \quad (2)$$

The choice for this test section pressure was made because it was found to provide sufficient imaging signal for the refractive index field as discussed below in §3. For a

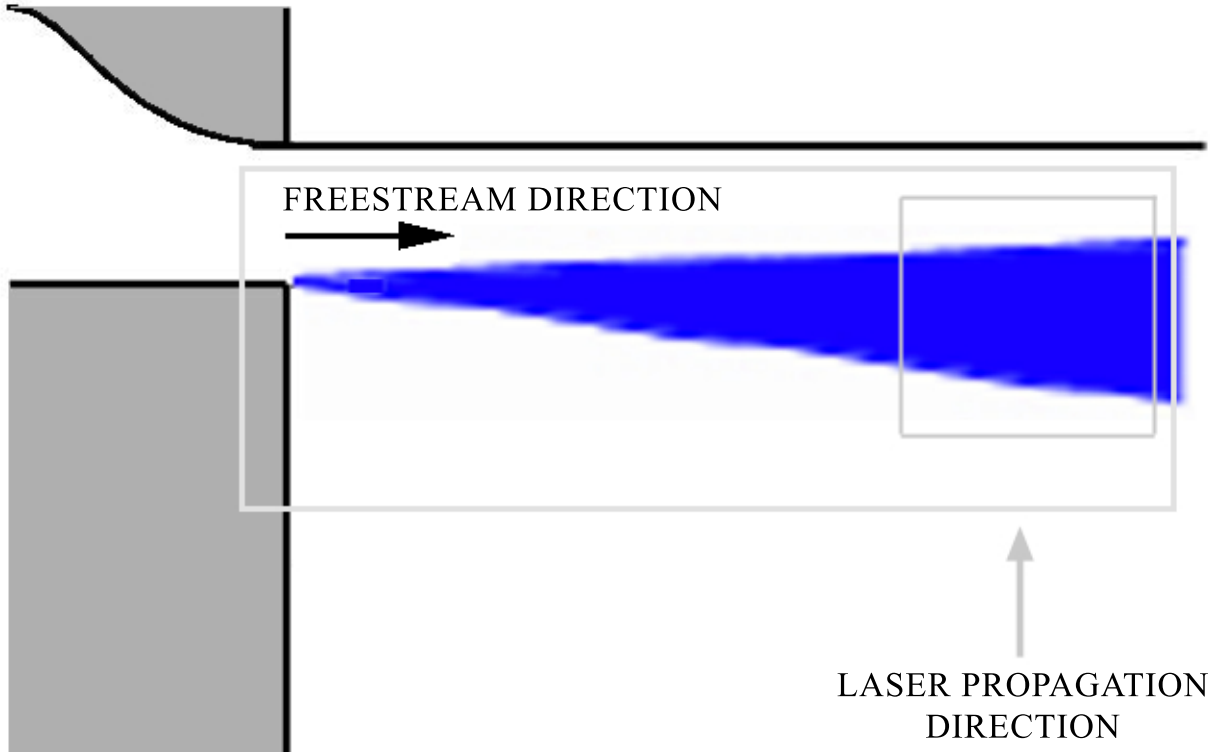


Figure 3: Schematic showing the separated free shear layer flow geometry and the laser propagation geometry. A convergent nozzle is employed with exit dimensions of $\sim 7.5\text{ cm} \times 30\text{ cm}$ to produce a subsonic freestream which separates past the 90° corner shown. The perpendicular wall below the separation point extends sufficiently vertically and spanwise to ensure ample entrainment of the ambient fluid. This feature, combined with zero downstream pressure gradient, ensures a separated free shear layer with linear growth rate and without reattachment. The larger and smaller rectangles shown indicate the extents of the fields of view used for the shadowgraphs and for the laser induced fluorescence images, respectively, in the present studies. In this schematic, the freestream direction is horizontal, from left to right, and the laser propagation direction is vertical, from bottom to top. The orientation in the experiments, with the vertical tunnel, is 90° counterclockwise to the orientation of this schematic, i.e. the actual flow orientation is vertical and the laser propagation direction is horizontal, cf. figures 1 and 2.

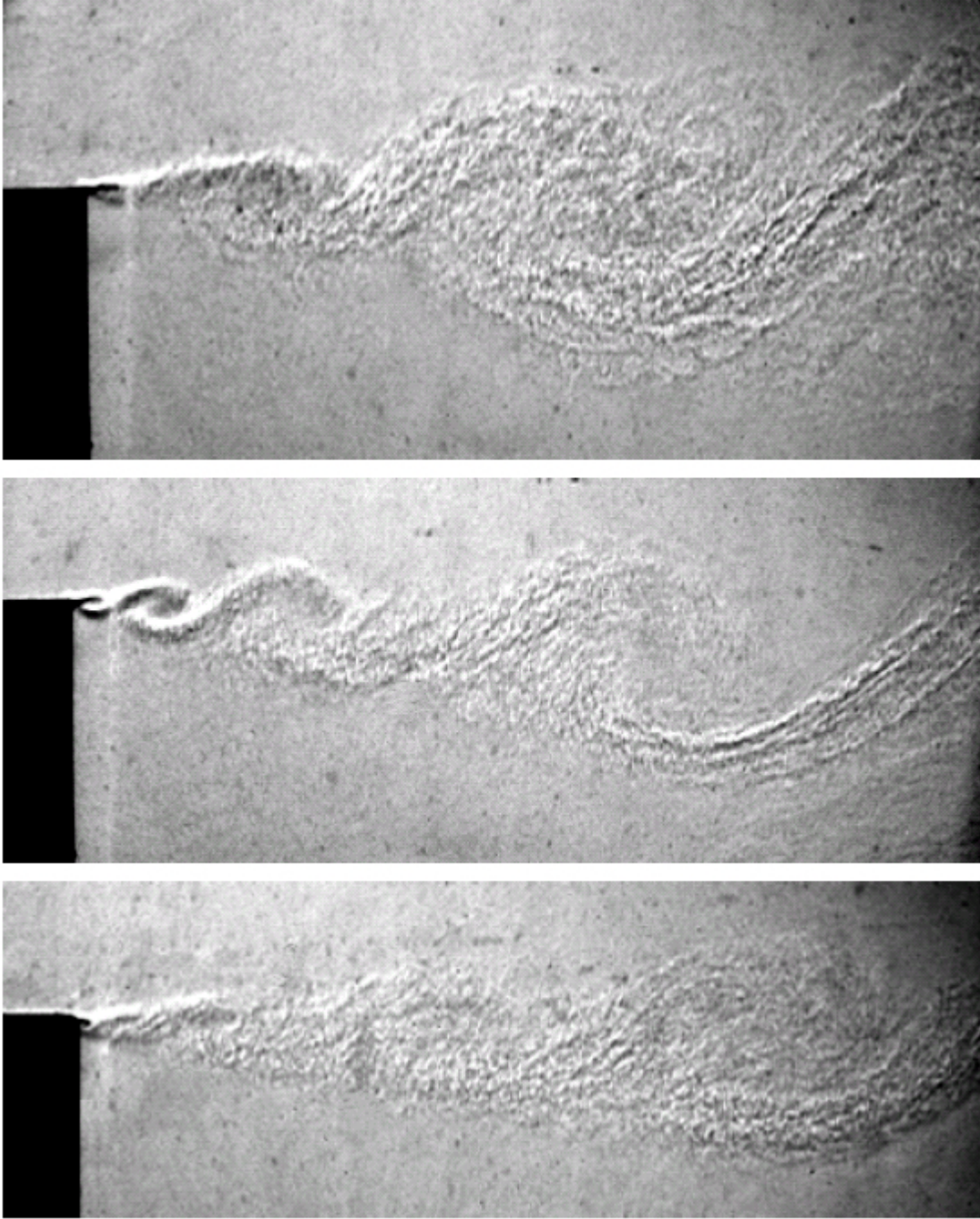


Figure 4: Whole field shadowgraphs of separated shear layers with increasing compressibility (from top to bottom). The top image is for a nearly incompressible shear layer, the middle image is for a convective Mach number of $M_c \sim 0.2$, and the lower image is for a convective Mach number of $M_c \sim 0.4$ with a Reynolds number of $Re \sim 6 \times 10^6$ based on the visual thickness at the right edge. The images show the aero-optical intensity variations for 10-inch diameter beams propagated spanwise normal to the shear layers. The freestream fluid is a purely gaseous air/acetone mixture, above each shear layer, and ambient air is below each shear layer. Large scale organized vortices with secondary braid vortices are evident in all images of these single-stream shear layers. The flow organization and the reduction of the growth rate with increasing compressibility are consistent with previous studies of two-stream shear layers [24, 27].

convective Mach number of $M_c \sim 0.4$, corresponding to the shadowgraph shown in the bottom in figure 4, the freestream Mach number is:

$$M_\infty \sim 0.9. \quad (3)$$

The growth rate $L' \equiv dL/dx$ of the compressible separated shear layer at $M_c \sim 0.4$ was found to be:

$$\frac{L'}{L'_{\text{inc.}}} \sim \frac{dL/dx}{dL_{\text{inc.}}/dx} \sim 0.6, \quad (4)$$

where $L'_{\text{inc.}} \equiv dL_{\text{inc.}}/dx$ is the growth rate for the incompressible separated shear layer. This is in agreement with previous studies of the effect of compressibility (e.g. [28, 29, 30, 31, 32, 33, 34, 35, 27, 36]).

The present study focuses on the flow conditions with $M_c \sim 0.4$ which is a moderate level of compressibility in shear layers (e.g. [27, 37]). In the context of aero-optics, the moderate compressibility conditions associated with $M_c \sim 0.4$ are directly relevant to practical flight conditions for airborne directed energy systems (e.g. [5, 9]). In the following sections, results are presented on laser induced fluorescence imaging of the refractive turbulent field (§3), the physical behavior of the refractive turbulent interfaces (§4), and physical modeling of the aero-optical interactions (§5), for $M_c \sim 0.4$.

In order to conduct direct imaging of the refractive turbulent field interfaces in purely gaseous flow, the present study utilizes acetone vapor to seed the air at a molecular level. This provides three significant advantages in comparison to other approaches. Firstly, the use of acetone vapor provides a significant laser induced fluorescence signal at elevated pressures [38, 39] in comparison to weaker signals such as those arising from Rayleigh scattering in air (e.g. [40]). Secondly, for the present flow imaging experiments, the acetone vapor is desirable because it ensures purely gaseous fluid in the test section and thus it provides a molecular marker in contrast to seeding with liquid droplets, fog particles, or smoke particles for example [41]. Thirdly, and most importantly regarding beam steering, whereas approaches using high Rayleigh scattering cross-section gases such as ethylene introduce highly undesirable intensity streaks (e.g. [6]), the present approach results in refractive index field images that are free of intensity streaks and thus eliminating any significant beam steering in the turbulent region of the flow. This is achieved by utilizing a relatively low seeding level of acetone vapor for the fluorescence imaging. The importance of streak-free imaging is that one does not have to resort to approximate methods of attempting to remove the streaks as was done in previous work [6]. Streak-free imaging of refractive fields provides a means to gauge whether or not significant beam steering occurs. In the present experiments, there is no evidence of intensity streaks in the laser-sheet images. This is because care was taken to ensure that sufficiently low seeding of acetone vapor in air was chosen. If there were significant beam steering occurring in the turbulent region of the flow, then there would be significant convergence and divergence of the laser rays and thus laser intensity streaks (non-uniformities) with higher intensities near beam convergence regions and lower intensities near beam divergence regions. Clear examples of significant beam steering and intensity streaks are evident in previous work [6]. Thus, if there were significant beam steering, then one would see intensity streaks generated in the laser sheet as it propagates through the refractive field. The absence of

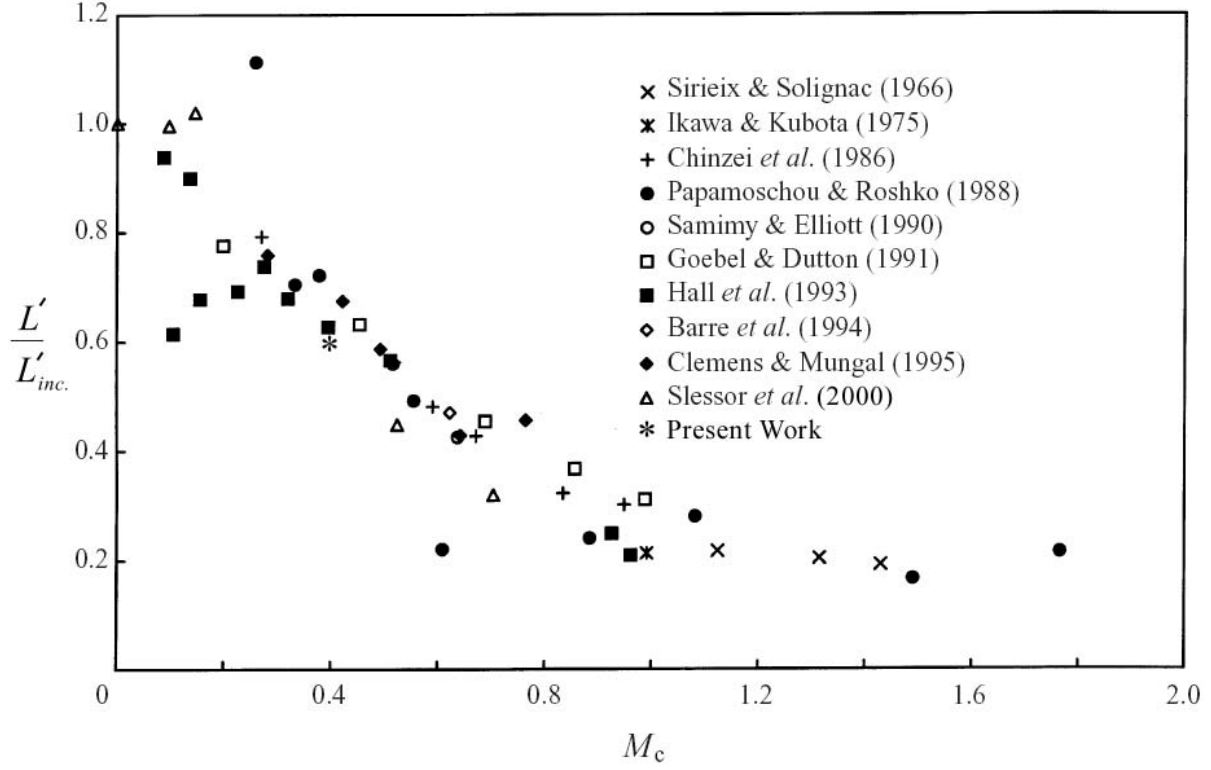


Figure 5: Compressibility scaling of the growth rate of the large scale visual thickness for the present work (asterisk symbol) and for previous studies (symbols as listed in legend) [28, 29, 30, 31, 32, 33, 34, 35, 27, 36]. The growth rate for the present primary compressibility condition of $M_c \sim 0.4$ is shown and is in accord with previous studies of compressibility effects.

intensity streaks in the present laser sheet images, such as figure 6 shown further below, is evidence that there is no significant beam steering.

In the present studies, acetone vapor molecularly mixed in air is generated by evaporating liquid acetone. To prepare the purely gaseous air/acetone mixture, a stream of air is passed through a liquid bath of acetone using the bubbling method [39]. The air/acetone mixture is supplied to the reservoir which is pressurized prior to each experimental run. The main vessel is pressurized with filtered air at $p \sim 3 \text{ atm}$ prior to exhausting the reservoir gas into the blow-down tunnel and test section. The acetone vapor concentration in air is regulated by controlling the mass flux of air through the bubbler. For the present experiments, an acetone vapor concentration of $\sim 2\%$ by volume is generated in order to ensure minimal absorption of the laser power, as shown in previous related experiments on laser induced fluorescence (e.g. [16]), and in order to maintain conditions below the lower flammability limit of acetone. Fluorescence of acetone vapor requires excitation by ultraviolet illumination as discussed below.

As indicated in figure 2, an ultraviolet beam is generated from a pulsed Nd:YAG laser. The illumination source employed is a moderate energy laser system (Spectra Physics Model INDI 40-10) which produces $\sim 70 \text{ mJ}$ per pulse at a wavelength of 266 nm . This ultraviolet wavelength corresponds to frequency quadrupling at the fourth harmonic of the fundamental infrared 1064 nm output of the laser. The laser beam is shaped into a laser sheet with a width of $\sim 15 \text{ cm}$ and a thickness of $\sim 150 \mu\text{m}$. A parabolic mirror ensures that the laser sheet that is produced is of parallel extent. The laser sheet is propagated through the quartz windows of the pressure vessel and into the high Reynolds number separated shear layer in the test section. The laser sheet orientation corresponds to a streamwise slice of the shear layer, cf. figure 3. The extent of the laser sheet that illuminates the shear layer is $\sim 15 \text{ cm} \times 15 \text{ cm}$. The laser sheet width of $\sim 15 \text{ cm}$ corresponds to the downstream extent of the imaged shear layer. The large scale transverse extent of the shear layer at the imaging location is $L \sim 10 \text{ cm}$. The incident laser sheet excites the acetone vapor in the air to generate visible (blue) fluorescence. The elevated test section pressure of $p \sim 3 \text{ atm}$ results in an increase in the fluorescence signal, relative to atmospheric or sub-atmospheric test section pressures, in agreement with previous studies [39].

The laser induced fluorescence imaging signal is recorded on a high resolution digital intensified charge-coupled device (CCD) camera with $\sim 1,000 \times 1,000$ pixels. The camera system is oriented along a direction normal to the laser sheet and, therefore, perpendicular to the incident laser propagation direction. The digital camera system employed is an intensified CCD camera by Stanford Photonics (Mega-10Z) with enhanced sensitivity in the blue spectrum. This enables the recording of the two-dimensional spatial slices of the acetone vapor concentration field. The fluorescence signal images are normalized and calibrated pixel-by-pixel using post-run images recorded at uniform concentration as well as pre-run images that correspond to pure air in the test section. The normalization and calibration procedure is similar to the method described in a previous study [16]. In the present experiments, the compressible turbulent mixing of the freestream gas with the ambient gas generates the refractive index field corresponding directly to the acetone vapor concentration field.

An example of a high resolution calibrated and normalized image of the refractive index field of the separated high Reynolds number shear layer is shown in figure 6, for the same flow conditions of $Re \sim 6 \times 10^6$, $M_c \sim 0.4$, and $p \sim 3$ atm. A total of twenty uncorrelated images were recorded at the same flow conditions. As indicated in the schematic of figure 3, the image shown corresponds to a two-dimensional spatial streamwise slice. The image provides the instantaneous refractive index field since the laser pulse temporal duration is $\lesssim 10$ nsec and thus faster than the shortest time scales of the flow. The colors shown in the image correspond to variations in the refractive index. Pure ambient air corresponds to the white region located at the bottom of the image. The freestream fluid is visible as dark blue in the upper region of the image. The intermediate colors correspond to mixed fluid. For these images, the signal-to-noise ratio is estimated from the measurements to be in excess of $\sim 100 : 1$ which is large enough to enable accurate extraction of fluid interfaces such as refractive index interfaces or high gradient interfaces. In flow imaging experiments of high Reynolds number flows [42, 6, 37, 12], there are resolution limitations associated with the finite number of camera pixels and with the finite laser sheet thickness. The present image data can be viewed as coarse-grained data which are useful for characterizing the large scale refractive index field behavior.

As is evident in the quantitative visualization in figure 6, a relatively sharp interface is present between the freestream fluid and the mixed fluid (upper part of image) as well as between the ambient fluid and the mixed fluid (lower part of image). This is consistent with previous investigations that have focused on the outer fluid interface between pure fluid and mixed fluid (e.g. [43, 6, 44, 16]). The sharpness of the outer interface is also consistent with theoretical considerations of diffusion (e.g. [45]). The outer interface is the dynamic interface whose location marks the extent of the mixed fluid region. The relative sharpness of the outer interface depends, in general, on both the Reynolds number and the Schmidt number. Although the Schmidt number for the present studies is of order unity, i.e. corresponds to relatively large molecular diffusion in comparison to mixing in liquids, the high Reynolds number provides the high small-scale strain rates which limit the local extent of molecular diffusion in the vicinity of the interface [44]. The pronounced vorticity/scalar correlations present in fully developed turbulent mixing maintain the sharpness of the outer interface (e.g. [16]).

A scalar field, such as the refractive index field $n(\mathbf{x}, t)$, can be physically represented in terms of its scalar interfaces. In the present case, the refractive index interfaces are diffusive interfaces across which molecular diffusion occurs. Also, in the context of aerodynamics, the interactions of the optical wavefronts with the fluid occur physically across these interfaces. Properties of turbulence-generated isosurfaces of scalar fields $q(\mathbf{x}, t)$, i.e. $q(\mathbf{x}, t) = \text{const.}$, have been examined previously for various flow conditions in the context of mixing and other applications (e.g. [15, 46, 16]). Associated with the refractive index field $n(\mathbf{x}, t)$, the refractive isosurfaces are given by:

$$n(\mathbf{x}, t) = \text{const.} \quad (5)$$

Although the isosurfaces are key flow elements for physical modeling of phenomena sensitive to interfacial behavior, the isosurfaces have mathematically zero thickness (e.g. [15]). Thus, it is desirable to consider and examine physical thickness aspects of these turbulent interfaces (e.g. [47]).



Figure 6: Laser induced fluorescence example of a high resolution direct quantitative image of the refractive index turbulent field in the large Reynolds number compressible separated shear layer, cf. the flow geometry schematic in figure 3. The imaging of the refractive field in purely gaseous flow is achieved using laser induced fluorescence of acetone vapor molecularly mixed in air. The Reynolds number is $Re \sim 6 \times 10^6$ based on the large scale visual thickness, the convective Mach number is $M_c \sim 0.4$, and the test section pressure is $p \sim 3 \text{ atm}$. The freestream is from left to right in the upper region. The colors shown correspond to the refractive index field and have been added to aid the eye in discerning the refractive turbulent interfaces. Dark blue is for the high-speed freestream (top) and white is for the ambient air (bottom).

Each refractive interface can be thought of as consisting of fluid residing between the two neighboring isosurfaces:

$$n(\mathbf{x}, t) + dn = \text{const.}, \quad \text{and}, \quad n(\mathbf{x}, t) = \text{const.}, \quad (6)$$

i.e. corresponding to the refractive indices $n + dn$ and n , respectively.

The local interfacial fluid thickness can be defined in terms of the refractive index gradient magnitude. From geometrical considerations, the refractive index gradient ∇n is normal to the interface at every point on the interface. As long as the magnitude $|\nabla n|$ of the gradient is finite, we can define the interfacial thickness h_n per unit n as:

$$h_n(\mathbf{x}, t) \equiv \frac{1}{|\nabla n|} = \left| \frac{\partial n}{\partial s} \right|^{-1}, \quad (7)$$

where s denotes distance along the local normal to the interface. The actual spacing between the isosurfaces, cf. equation 6, is therefore $h_n dn$. This corresponds to the full interfacial thickness.

By general geometrical considerations, we can express the differential volume $dV(n)$ of fluid residing between these two neighboring isosurfaces as:

$$\frac{dV(n)}{V_{\text{ref}}} \equiv \frac{A(n)}{V_{\text{ref}}} \bar{h}_n dn, \quad (8)$$

where $A(n)$ is the interfacial surface area, V_{ref} is a reference volume, and $\bar{h}_n dn$ is the mean spacing between the neighboring isosurfaces which can be interpreted as the mean interfacial thickness.

It can be noted that, since the values of the refractive index field are dimensionless, the quantity h_n has the units of length. For simplicity, therefore, we will refer to h_n as the interfacial thickness. As a result of the strong intermittency of turbulent flows (e.g. [48], [47]), especially at high Reynolds number flow conditions, the local interfacial thickness can be expected to be highly variable.

The interfacial fluid thickness h_n for the present data was computed on the basis of equation 7. Since, in the present measurements, only two-dimensional spatial information is available for the refractive index field, only the in-plane component of the full interfacial thickness can be evaluated. This is shown in figure 7. Evaluation of the full value of the interfacial thickness would require the three-dimensional refractive index gradient (e.g. [49]). Nevertheless, the two-dimensional information is useful in the context of aero-optical interactions in terms of characterizing the in-plane optical phase distortions as demonstrated in previous studies (e.g. [6, 10]).

The behavior in figure 7 indicates the presence of high gradient interfaces, denoted as dark regions in the figure. These high gradient interfaces are highly irregular and are present at the outer boundaries between mixed fluid and pure fluid as well as in the interior. These networks of relatively isolated high gradient interfaces, in these two-dimensional images, are consistent with previous observations of sheet-like structures in

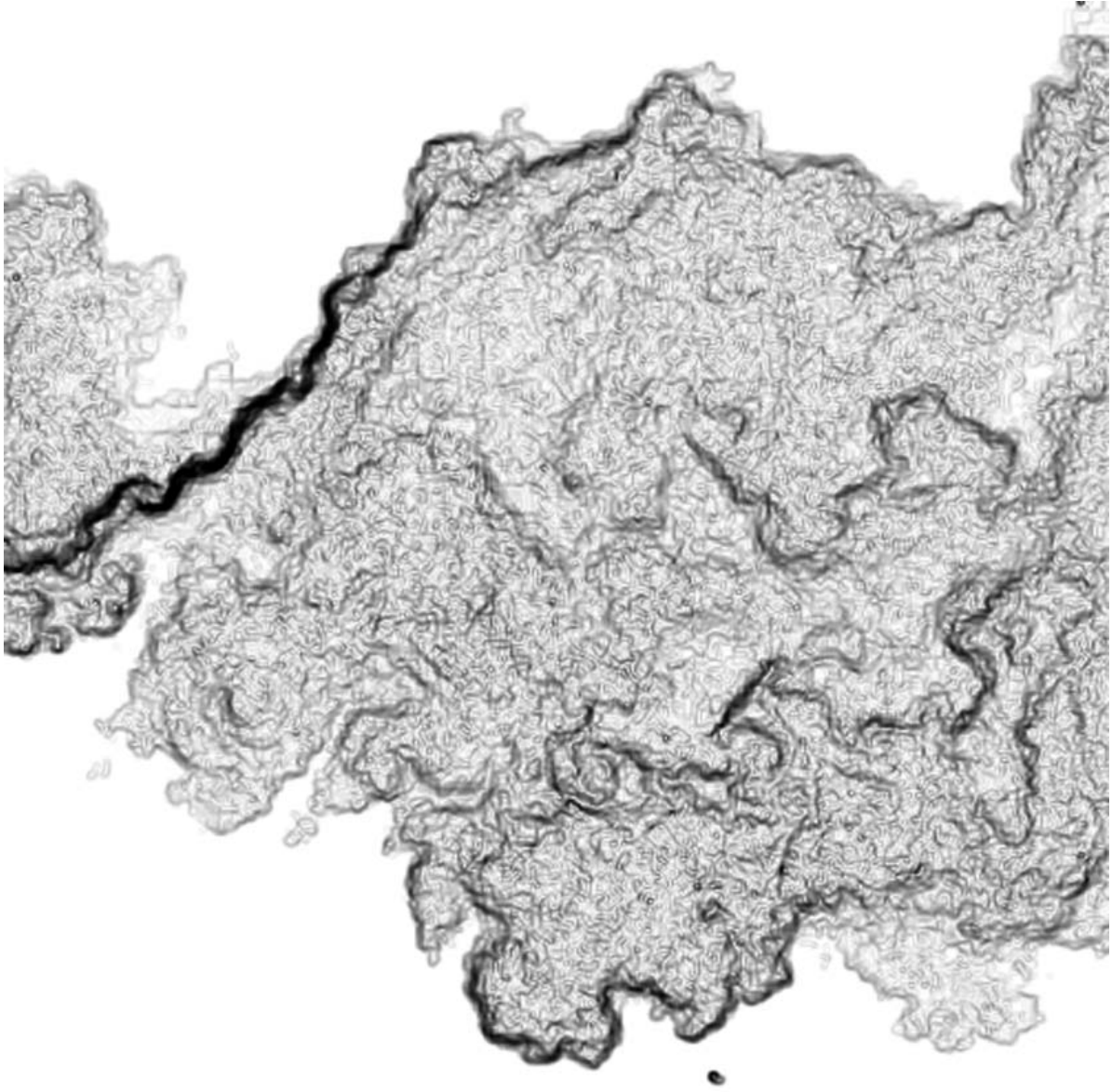


Figure 7: Example of the in-plane components of the interfacial fluid thickness h_n corresponding to the refractive index image shown in figure 6. The interfacial thickness field shown was computed based on equation 7 for the two in-plane components. The magnitude of the interfacial thickness is labeled with grey values. Darker regions denote higher gradient locally thinner interfaces. Highly irregular networks of high gradient interfaces are evident both in the interior of the flow and at the outer boundaries.

three dimensions in the scalar dissipation rate field (e.g. [49, 50]). It can be appreciated, in general, that the wide range of interfacial scales at high Reynolds numbers prevents direct examination of the entire range of thickness scales. At finite resolution, such as with the present data, the available refractive index field corresponds to a coarse-grained field with information retained only at or above the resolution scale (e.g. [12]).

Knowledge of the refractive index field is useful both for evaluating the optical wavefront distortions and for identifying the dominant fluid interfaces in the aero-optical interactions (e.g. [6, 9]). Evaluation of the wavefront distortions, given information on the refractive interfaces, depends on the flow regime and optical regime. For example, near-field interactions are well described by geometrical optics while far-field interactions require wave descriptions based on Maxwell's equations (e.g. [7, 51]). Also, for high energy beam propagation there is two-way coupling between the fluid and the optical waves, whereas for low energy beams there is only one-way coupling between the flow structure and the beam distortion (e.g. [52, 53, 6]).

For the present studies, the measured refractive index fields are utilized with the eikonal equation of geometrical optics to propagate computationally the optical wavefronts in the near field. As long as the smallest turbulent scales are greater than the optical wavelength scales (e.g. [54]), the geometrical optics description is sufficient for near-field aero-optical interactions. In terms of the refractive index field n and the optical path length (OPL), the eikonal equation is:

$$|\nabla(\text{OPL})| = n, \quad (9)$$

(e.g. [55]). Solutions of this equation along the individual ray paths correspond to the OPL integral in terms of the refractive index field:

$$\text{OPL}(\mathbf{x}, t) \equiv \int_{\text{ray}} n(\ell, t) d\ell. \quad (10)$$

The OPL integral corresponds to inverting the eikonal equation 9. The physical distance along the beam propagation path for each light ray is denoted as ℓ .

The optical wavefronts can be represented as isosurfaces of the OPL, i.e.,

$$\text{OPL}(\mathbf{x}, t) = \text{const.} \quad (11)$$

The OPL also corresponds to the optical phase or wavefront propagation time (e.g. [1]). A useful way to quantify the wavefront distortions is in terms of the optical path difference (OPD) given by:

$$\text{OPD}(\mathbf{x}, t) \equiv \text{OPL}(\mathbf{x}, t) - \overline{\text{OPL}}, \quad (12)$$

where $\overline{\text{OPL}}$ corresponds to the ensemble averaged OPL value. A useful measure of the wavefront distortion is the root-mean-square (rms) value of the OPD variations, i.e.:

$$\text{OPD}_{\text{rms}} \equiv \left(\left\langle \left| \text{OPD}(\mathbf{x}, t) \right|^2 \right\rangle_{\text{ens.}} \right)^{1/2}, \quad (13)$$

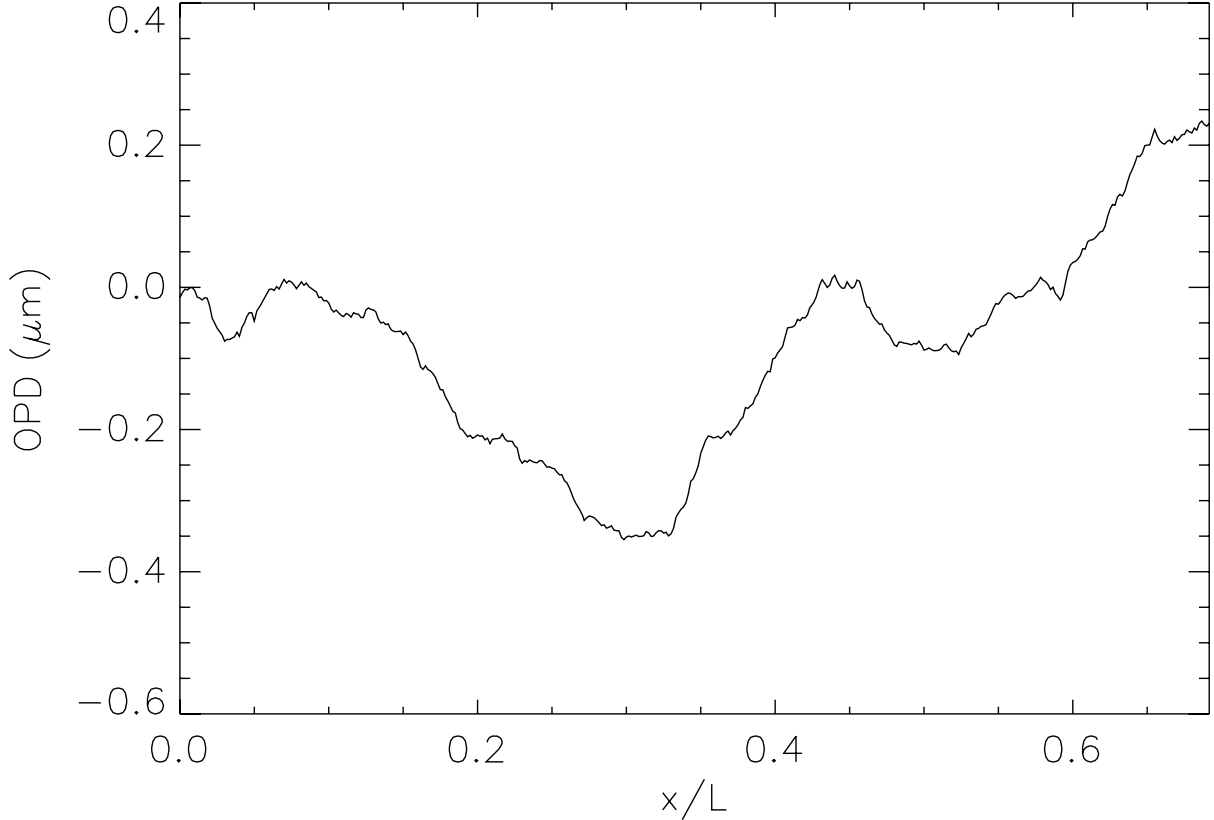


Figure 8: Flow-derived optical wavefront phase profile evaluated at the upper boundary of the field of view of the refractive index field image shown in figure 6. The streamwise distance is normalized in terms of the large scale visual thickness of the flow. The ensemble averaged root-mean-square optical path difference (OPD_{rms}) was found to be in agreement with independent Shack-Hartmann measurements of the aero-optical aberrations at the same flow conditions.

where $\langle \rangle_{\text{ens.}}$ denotes ensemble averaging. The ensemble averaged OPD value for wavefronts corresponding to the present database of images was found to be:

$$\text{OPD}_{\text{rms}} \approx 0.2 \mu\text{m}. \quad (14)$$

Independent Shack-Hartmann measurements of the aero-optical aberrations were conducted and found to also result in an ensemble averaged value of $\text{OPD}_{\text{rms}} \approx 0.2 \mu\text{m}$, i.e. in agreement with the flow-derived value of OPD_{rms} . It must be noted that this OPD_{rms} value is for the present flow conditions. In general, it can be expected to be a function of Reynolds number, Mach number, flow geometry, and other parameters. The OPD_{rms} value can be used to normalize the OPD profile for each distorted wavefront. Also, this quantity is directly related to a measure of beam attenuation known as the Strehl ratio which is a key quantity for evaluating the effects of the refractive index field on the peak intensity of the propagated beam [1, 6].

Using the present measurements of the refractive index field n and equation 10, the evolution of the wavefront OPD through the cross-section of the shear layer can be examined. Figure 8 shows an optical wavefront phase profile corresponding to the upper

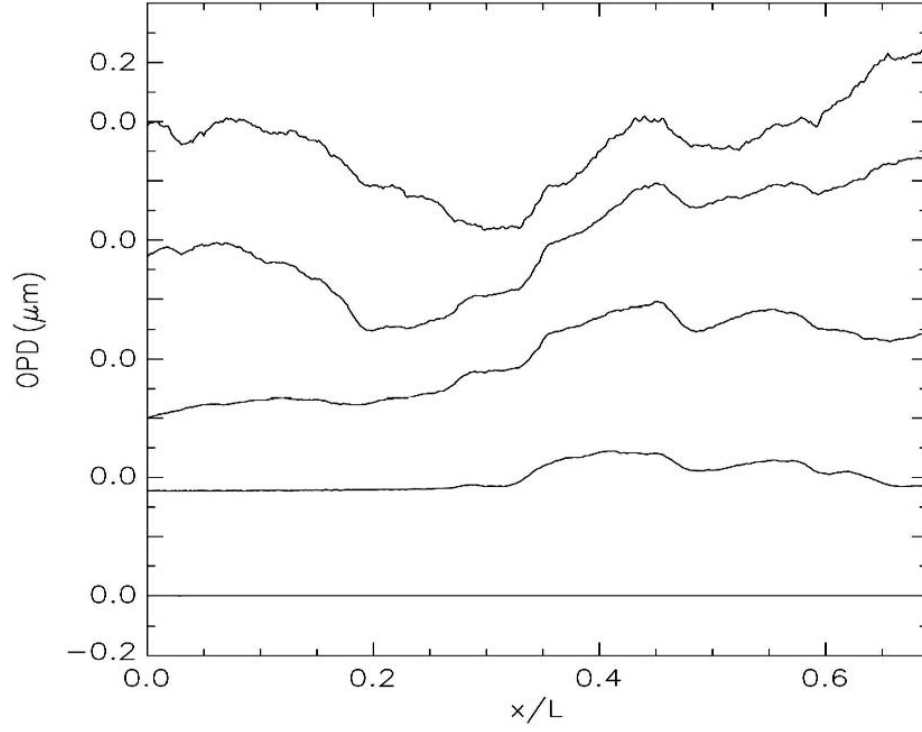


Figure 9: Results of the evolution (top) of the optical path difference (OPD) for wavefronts propagating through the refractive field (bottom) of the high Reynolds number compressible separated shear layer, using the image data in figure 6 reproduced here for comparison. Successive OPD profiles are shown at several transverse distances through the flow, with the wavefronts propagating vertically from bottom to top.

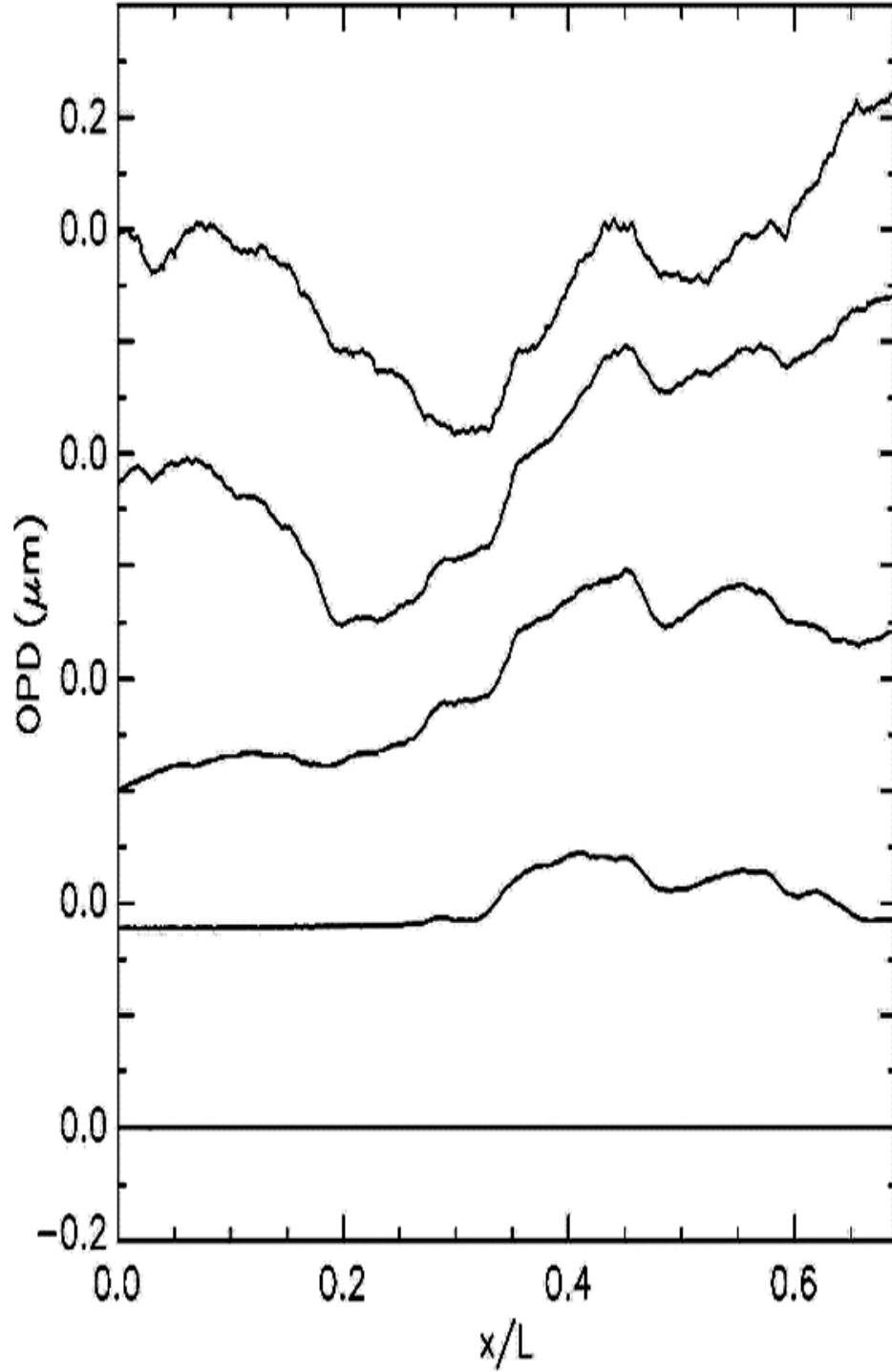


Figure 10: Expanded visualization of the top part of figure 9 for the cumulative behavior of the OPD for optical wavefronts propagating through the compressible separated shear layer. As stated for figure 9, successive OPD profiles are shown at several transverse distances through the flow, with the wavefronts propagating vertically from bottom to top. The streamwise distance is normalized by the large scale visual thickness of the flow. The uppermost OPD profile was evaluated at the upper boundary of the field of view of the refractive-index field. The ensemble-averaged root-mean-square optical path difference (OPD_{rms}) was found to be consistent with independent Shack-Hartmann measurements of the aero-optical aberrations at the same flow conditions.

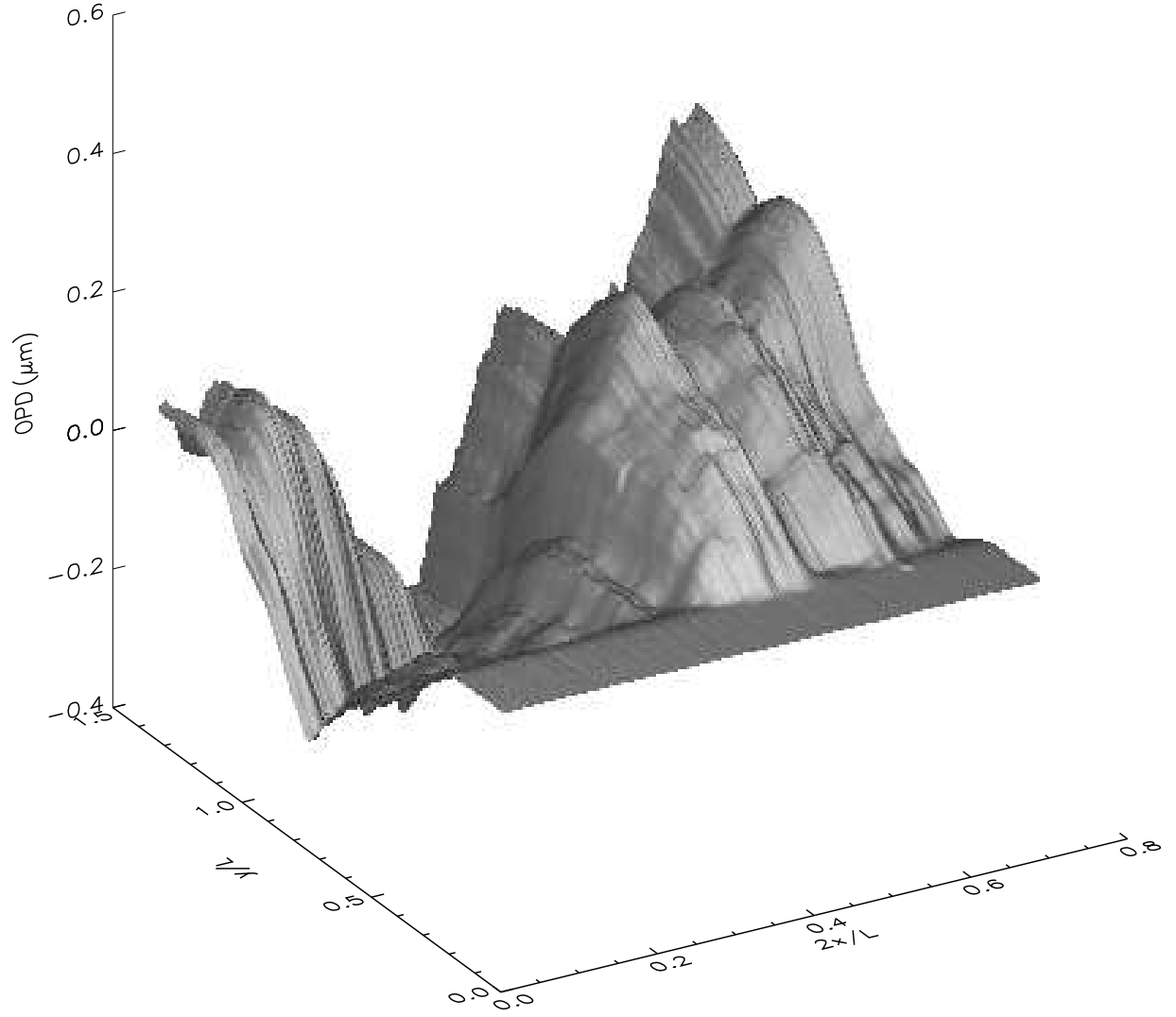


Figure 11: Surface depicting the evolution of the shape and distortion of the optical wavefront phase profile as it propagates through the shear layer along the entire beam propagation path contained in the turbulent flow region. The vertical axis corresponds to the optical path difference. This aero-optical interaction corresponds to figure 9.

boundary of the field of view of the refractive index field image shown in figure 6. Figure 9 (top) shows successive profiles of the OPD at several transverse locations through the shear layer, for planar incident wavefronts. The corresponding refractive index field is shown on the bottom in figure 9, reproduced from figure 6, to facilitate the visual inspection of the aero-optical interactions. The wavefront is propagated vertically, from bottom to top, in figure 9 (upper part). The first OPD profile, near the bottom of the sequence, has planar structure since it has not yet entered the shear layer and thus corresponds purely to the incident wavefront. The second OPD profile from the bottom of the sequence shows the initial distortion of the rightmost part of the wavefront as it passes through the sharp outer interface of the shear layer. Additional large scale features imposed on the wavefront structure by the shear layer interfaces are evident as the wavefront propagates further into the shear layer. These are evident, for example, in the upper three profiles in the sequence. Successive nearly-uniform large scale regions, or plateaus, in the refractive index field separated by irregular high gradient interfaces appear to form a primary mechanism in the observed aero-optical interactions. The entire evolution of the wavefront shape is shown in figure 11. The observed behavior in the OPL profile sequence demonstrates the utility of refractive index field imaging to examine the role of the refractive interfaces in the aero-optical interactions.

The structure of the refractive index field and its effect on the propagation of the wavefronts, as depicted for example in the sequence in figure 9, suggests that the dominant contributions to the wavefront distortions can be identified in terms of the high gradient refractive interfaces. To do so, one can utilize the physical thickness $h_n(\mathbf{x}, t)$ of the interfaces as defined above in equation 7.

The role of the thickness of the refractive interfaces in the aero-optical interactions can be seen directly by expressing the OPL in equation 10 as an integral with respect to the refractive index n rather than the propagation distance ℓ , i.e.

$$\text{OPL}(\mathbf{x}, t) \equiv \int_{\text{ray}} n(\ell, t) h_{n,\ell} |dn|, \quad (15)$$

where $h_{n,\ell}$ is the interfacial thickness component in the direction of optical propagation:

$$h_{n,\ell} = \frac{1}{|\nabla n|_\ell}. \quad (16)$$

This takes into account the orientation of the interface relative to the light ray direction, with $|\nabla n|_\ell$ denoting the component of the magnitude of the refractive index gradient in the ℓ direction, i.e. in the direction of the optical ray propagation, i.e.

$$|\nabla n|_\ell \equiv \left| \frac{\partial n}{\partial \ell} \right|, \quad (17)$$

The absolute values in equations 15 and 17 are needed since the refractive index n could be locally increasing or decreasing as the light rays propagate.

Whenever the interfaces are not normal to the optical rays, the gradient magnitude component will be smaller than the full gradient magnitude and therefore the interfacial

thickness through which the ray propagates will be effectively larger. If a part of a refractive interface is locally normal to an optical ray, the gradient component $|\nabla n|_\ell$ will be the same as the full gradient magnitude $|\nabla n|$. Thus, in general, the gradient magnitude component must always be less than or equal to the full gradient, i.e.

$$|\nabla n|_\ell \equiv |\nabla n| |\cos \theta| \leq |\nabla n|, \quad (18)$$

which means that the effective interfacial thickness must always be greater than or equal to the full thickness, i.e.

$$h_{n,\ell} = \frac{1}{|\nabla n|_\ell} \equiv h_n |\sec \theta| \geq h_n. \quad (19)$$

The angle θ , taken as $-\pi < \theta \leq \pi$, quantifies the orientation of the refractive index gradient, which is always normal to the fluid interface, relative to the local optical propagation direction. It can be noted that the above relations, as written, require that the local gradient magnitude is finite, i.e. $|\nabla n| \neq 0$. They can be modified, in a straightforward manner, in any regions of uniform refractive index, i.e. regions of $|\nabla n| = 0$. For example, $h_{n,\ell} |dn|$ can be interpreted as a Dirac delta function whose integral is the extent $\Delta\ell$ of the uniform index region in the optical propagation direction, and its contribution to the OPL integral becomes $\Delta(\text{OPL}) = n \Delta\ell$, in that case.

The role of the interfacial thickness enables a physical model for the large scale aero-optical interactions, by appreciating that the high gradient locally-thin interfaces provide the dominant contributions to the wavefront distortions. Figure 12 shows the comparison between the full OPD profile and a modeled OPD profile where a gradient threshold is employed to retain only $\sim 50\%$ of the original refractive index field values that correspond to local gradients above the threshold. For the ensemble averaged data, there is less than $\sim 10\%$ difference in the root-mean-square OPD at the present flow conditions. Because the high gradient interfaces are spatially isolated, as is evident in the image in figure 7, the low gradient regions in between the high gradient interfaces are modeled to a first approximation as uniform index regions using the gradient at each boundary through which each ray propagates. It is helpful to appreciate that although the high gradient interfaces have a relatively small component $h_{n,\ell}$ of the thickness, they contribute significantly to the OPL integral in equation 15 because the differential $|dn|$ of the refractive index is relatively large across such interfaces. In this study, only the in-plane components of the interfacial thickness are available and thus figure 12 corresponds to the in-plane optical wavefront distortions only. The out-of-plane component would be needed to capture the out-of-plane wavefront distortions.

The present approach enables an examination of the effect of filtering the refractive field, i.e. by retaining only high gradient interfaces, on the optical wavefront phase aberrations for a wide range of filter values. Figure 13 shows the manner in which the difference in the root-mean-square OPD, between the full wavefront phase profiles and the modeled wavefront phase profiles, depends on the amount of reduction in the refractive field information as a result of the filtering. The percentage values of refractive field information reduction correspond to the extent of the filtered regions of the refractive field, i.e. the regions excluded as a result of modeling by retaining only high gradient interfaces. Higher

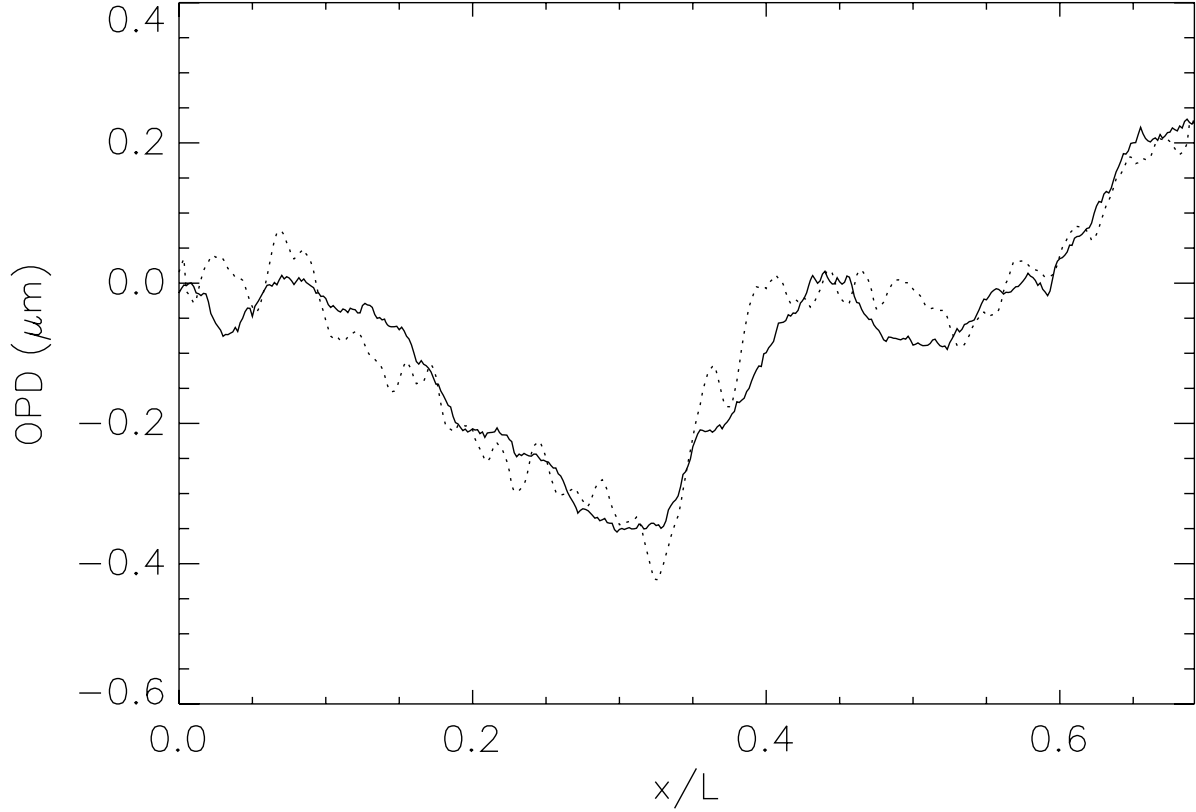


Figure 12: Modeled OPD profile (dotted curve) compared to the full OPD profile (solid curve), corresponding to the wavefront propagated through the separated shear layer in figure 9. The modeled OPD profile is computed using a modeled refractive index field consisting of high gradient interfaces, with low gradient regions replaced by uniform index regions, where the gradient threshold employed retains only $\sim 50\%$ of the original refractive index field values. For the ensemble averaged data, a difference of $\sim 10\%$ is observed in the root-mean-square OPD, between the modeled wavefront profiles and the full wavefront profiles, at the present flow conditions.

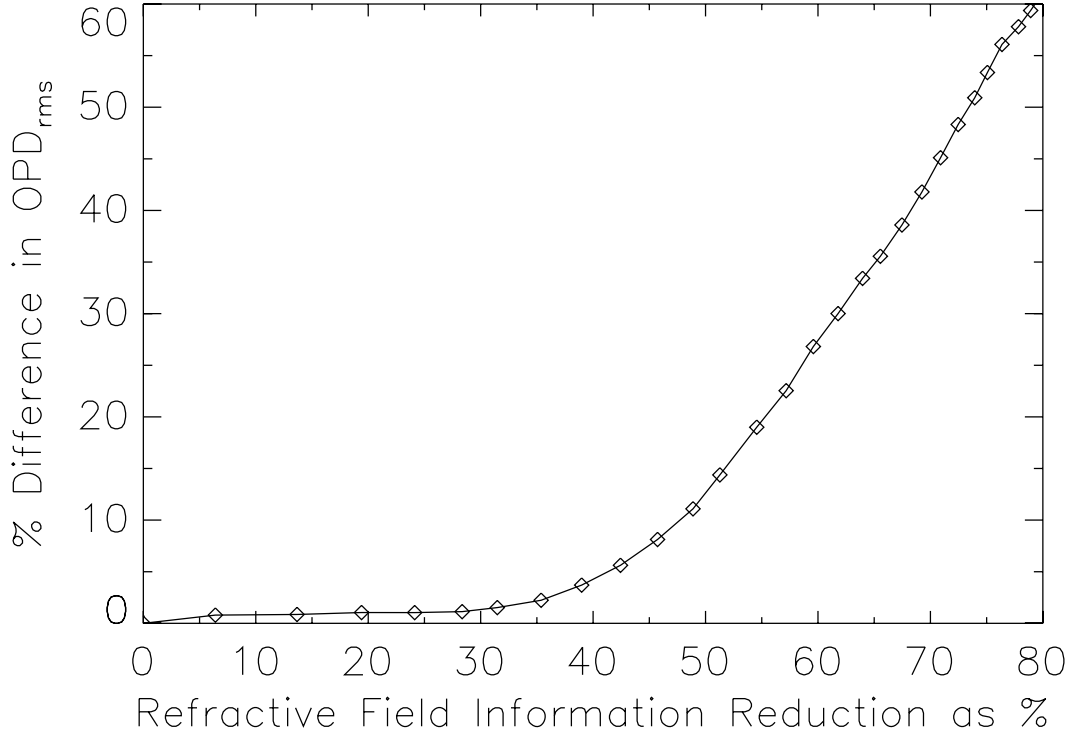


Figure 13: Dependence of the difference in the root-mean-square OPD, between the full wavefront phase profiles and the modeled wavefront phase profiles, on the amount of reduction in the refractive field information. The percentage of refractive field information reduction corresponds to the extent of the regions of the refractive field modeled by retaining only high gradient interfaces. Higher percentages of reduction in refractive field information correspond to higher gradient thresholds below which the refractive field is filtered. The difference of $\sim 10\%$ in the root-mean-square OPD for a gradient threshold resulting in $\sim 50\%$ reduction in refractive field information corresponds to the profiles shown in figure 12.

percentage values of reduction in refractive field information correspond to higher values of the gradient threshold below which the refractive field is filtered. Significant robustness is evident whereby less than $\sim 5\%$ difference in the root-mean-square OPD results for reductions of up to $\sim 40\%$ in the refractive field information. For reduction percentage values of up to $\sim 50\%$, less than $\sim 10\%$ difference in the root-mean-square OPD is evident. This robustness can be understood by appreciating that it is the high gradient interfaces that produce the dominant aero-optical interactions. The observed robustness provides a key ingredient that can be utilized in physical descriptions, modeling, as well as optimization studies in aero-optics.

To gain further insight into the one-to-one aero-optical correspondence as a function of distance z along the beam propagation path, we consider the cumulative optical path length. In other words, we consider the cumulative integral in terms of the refractive-index field, as a function of the beam propagation path distance:

$$\text{OPL}(z, t) \equiv \int_{\text{path}}^z n(\ell, t) d\ell \equiv \int_{\text{path}}^z n(\ell, t) h_{n,\ell} |dn|, \quad (20)$$

where $h_{n,\ell}$ denotes the interfacial thickness component in the ray direction along the beam path.

We can now consider a cumulative Strehl ratio in terms of the cumulative OPD_{rms} , i.e. in terms of the cumulative root-mean-square of the optical path difference as follows:

$$\text{SR}(z, t) = \frac{I(z, t)}{I_0}, \quad (21)$$

so that:

$$\text{SR}(z, t) \simeq \exp \left[- \left(\frac{2\pi \left\langle \int_{\text{path}}^z n(\ell, t) h_{n,\ell} |dn| \right\rangle_{\text{rms}}}{\lambda} \right)^2 \right]. \quad (22)$$

This cumulative Strehl ratio is a useful quantity that can enable examination of the one-to-one aero-optical correspondence and cumulative effects along the beam propagation path.

Figure 14 shows examples of results on the cumulative aero-optical behavior, i.e. as a function of distance along the dynamic beam propagation path. The plot in the top part of figure 14 shows the cumulative OPD_{rms} as a function of propagation distance for an individual flow realization. This is a non-monotonic function with increasing propagation distance for the instantaneous flow realization. The behavior reflects, physically, the result of different parts of the wavefront accumulating distortions at different rates. The plot in the bottom part of figure 14 depicts the cumulative Strehl ratio as a function of propagation distance. The non-monotonicity again reflects the result of different parts of the wavefront dynamically accumulating distortions that can collectively decrease as well as increase the Strehl ratio, cf. equation 22. The observed behavior in figure 14 is a new key feature that, as can be appreciated, can only be detected by examining the cumulative aero-optical interactions along the beam propagation path. In other words,

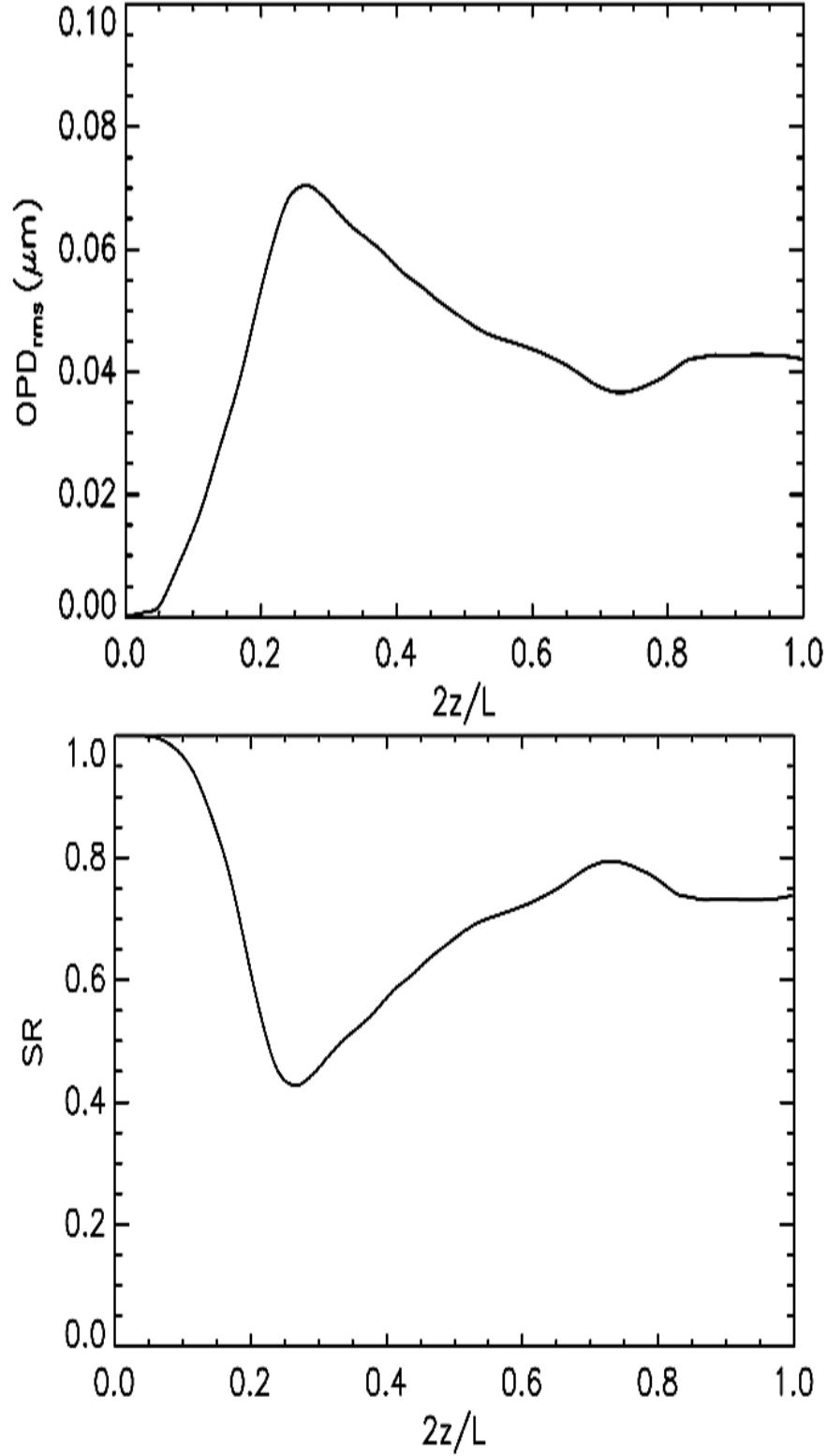


Figure 14: Top: Cumulative r.m.s. optical path difference OPD_{rms} , as a function of propagation distance, for dynamic laser sheet propagation through a large-Reynolds-number separated shear layer. Bottom: Cumulative Strehl ratio SR as a function of propagation distance corresponding to the r.m.s. optical path difference shown at the top.

knowledge of the integrated behavior only would have been insufficient to discover this. It is the direct, i.e. non-integrated, flow imaging that enabled the present finding.

The present observation and finding provide a key new aspect of aero-optical interactions for the aperture-integrated beam behavior, i.e. for finite-aperture beams. The extent to which this occurs in other flow realizations and at other flow conditions is an important future direction of research. The study of this will be facilitated with the interfacial-fluid-thickness (IFT) framework pioneered by the PI in previous AFOSR work [10] to identify the role of the high-gradient locally-thin interfaces in generating the dominant contributions to the wavefront distortions. The present results provide new insight into the mechanism by which one-to-one aero-optical interactions along the entire beam propagation path produce, cumulatively, the aberrations of the propagated laser beam. This new mechanism provides a key ingredient which can be expected to facilitate the development of aero-optical optimization techniques, including active forcing by plasma excitation to modify the primary refractive interfaces in order to reduce directly the beam aberrations.

In the research reported in this grant period, an additional key focus is on multiresolution aspects of the aero-optical interactions. The motivation is twofold. Firstly, multiresolution properties are useful to quantify the relative contributions of the large scales vs. the small scales. Secondly, the extent to which the large scales dominate the aero-optical interactions is useful for development of methods for reduction of beam aberrations such as the two principal approaches on flow control summarized above and changes in the flow geometry. In the results presented below, we examine the effect of modifying the resolution of the refractive-index field for various resolutions. These coarse-grained fields are then utilized to examine the resolution effect, i.e. the extent to which there is sensitivity or robustness, on the aero-optical interactions and aberrations.

As a reminder, we note that one of the key features of the work reported in this grant period is the combination of an experimental approach with a computational approach in order to examine the aero-optical interactions along the beam propagation path, retaining the large-Reynolds-number capability of the experiments while including the benefits of computations. We confine our discussion to the near-field aero-optical distortions for which geometrical optics provides a useful approximation [7], whereas far-field optical beam propagation requires Fourier optics. The present combined experimental/computational approach can be appreciated by realizing that in purely-computational aero-optics, [52, 60, 21, 53, 7, 51, 8] as in computational fluid dynamics, there are currently limitations regarding the Reynolds numbers that are achievable even with massively-parallel computers in direct numerical simulation (DNS) techniques. Current computations are limited to moderate Reynolds numbers unless subgrid-scale modeling is employed as in large-eddy simulations (LES). In contrast, whole-field imaging experiments such as in the present study at large Reynolds numbers and at finite resolution provide large-eddy experimental results free from any subgrid-scale modeling.

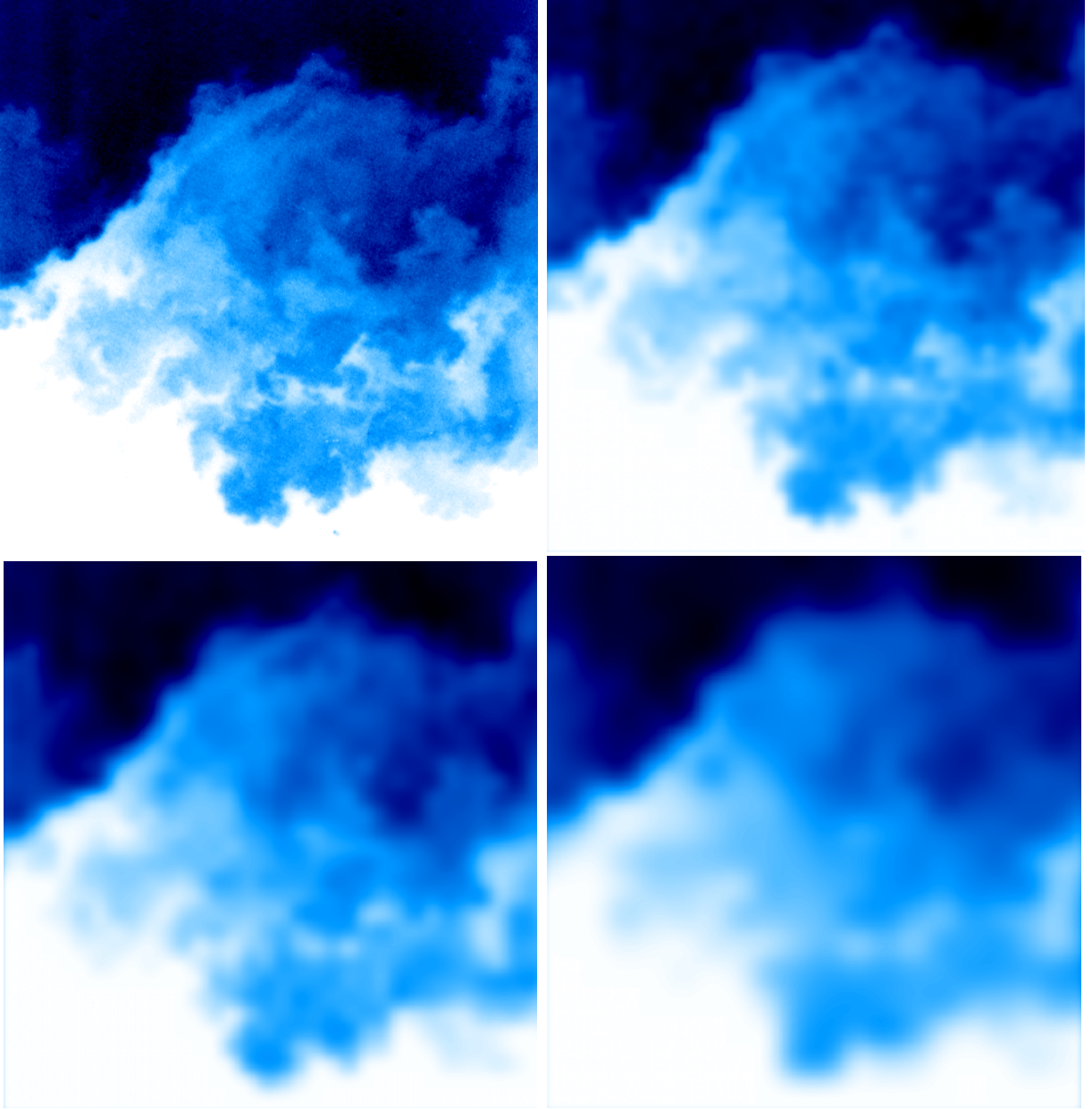


Figure 15: Top Left: Experimental refractive field image at a full resolution of $\sim 1000 \times 1000$ pixels for the compressible separated shear layer with $Re \sim 6 \times 10^6$, $M_c \sim 0.4$, and $p \sim 3$ atm. This image corresponds to laser-induced fluorescence arising from aero-optical mixing effects as opposed to density effects. Top Right: Reduction of the resolution to $\sim 75 \times 75$ pixels produced by coarse graining the original experimental high-resolution refractive field image. Bottom Left: Reduction of the resolution to $\sim 50 \times 50$ pixels produced by coarse graining the original experimental high-resolution refractive field image. Bottom Right: Reduction of the resolution to $\sim 30 \times 30$ pixels produced by coarse graining the original experimental high-resolution refractive field image.

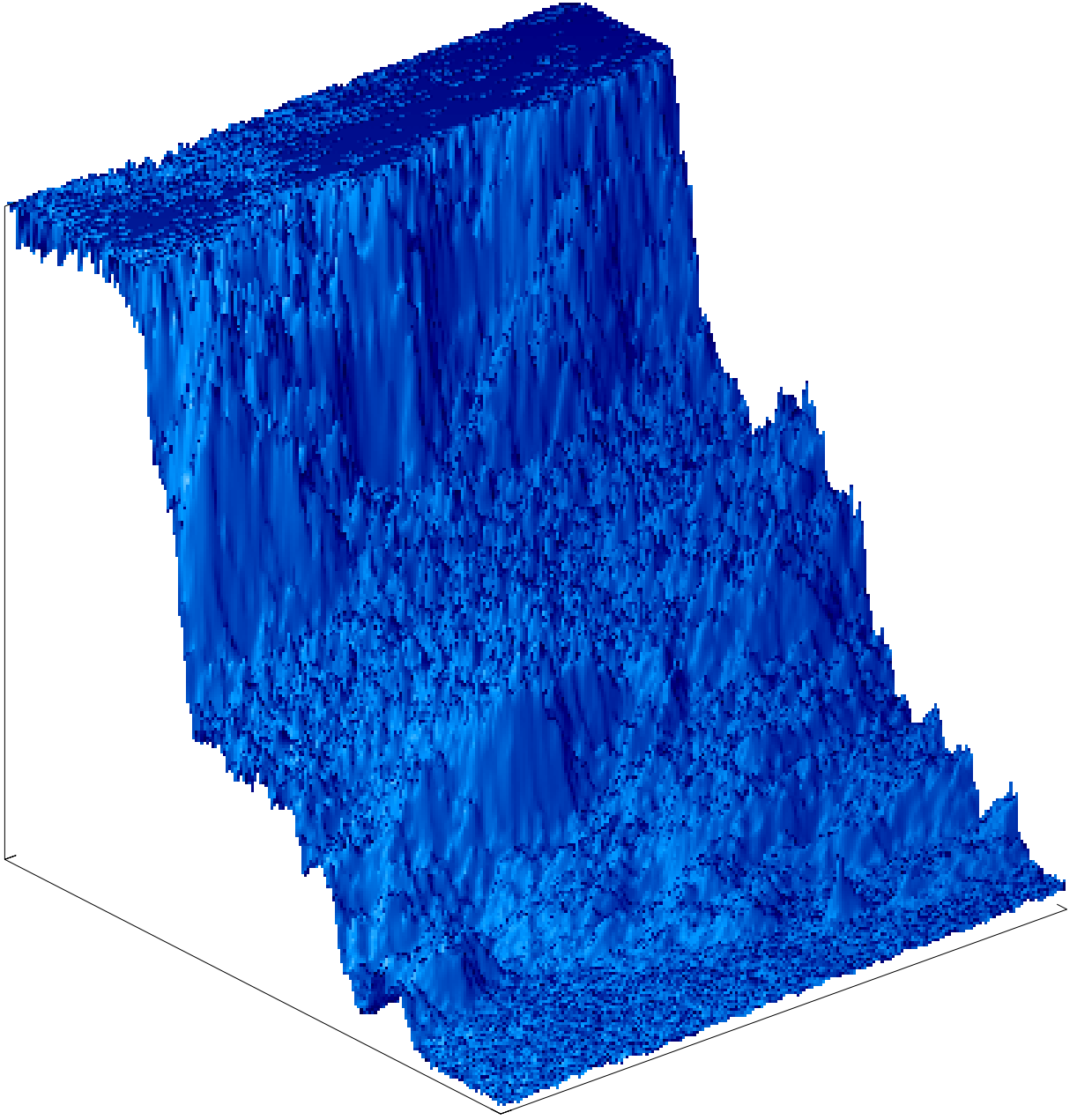


Figure 16: Surface rendering of the two-dimensional spatial refractive index field for the middle vertical third of the image in the top left of figure 15, at a spatial resolution of 150×600 pixels. This surface shows the variations of the refractive index across the transverse instantaneous extent of the shear layer encountered by the laser wavefronts.

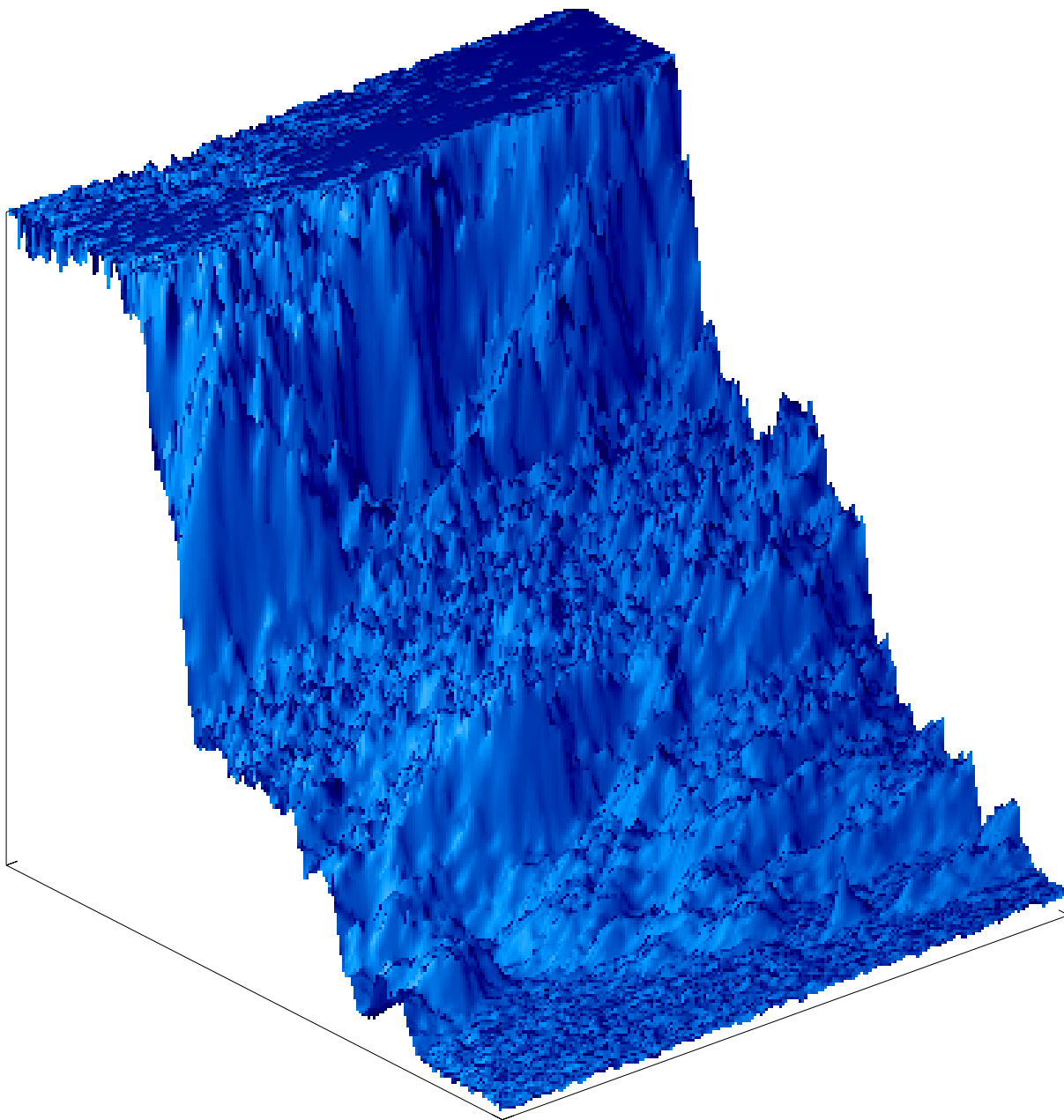


Figure 17: Surface rendering of the two-dimensional spatial refractive index field for the middle vertical third of the image in the top right of figure 15, at a spatial resolution of 100×400 pixels. This surface shows the coarse-grained variations of the refractive index across the transverse instantaneous extent of the shear layer encountered by the laser wavefronts.

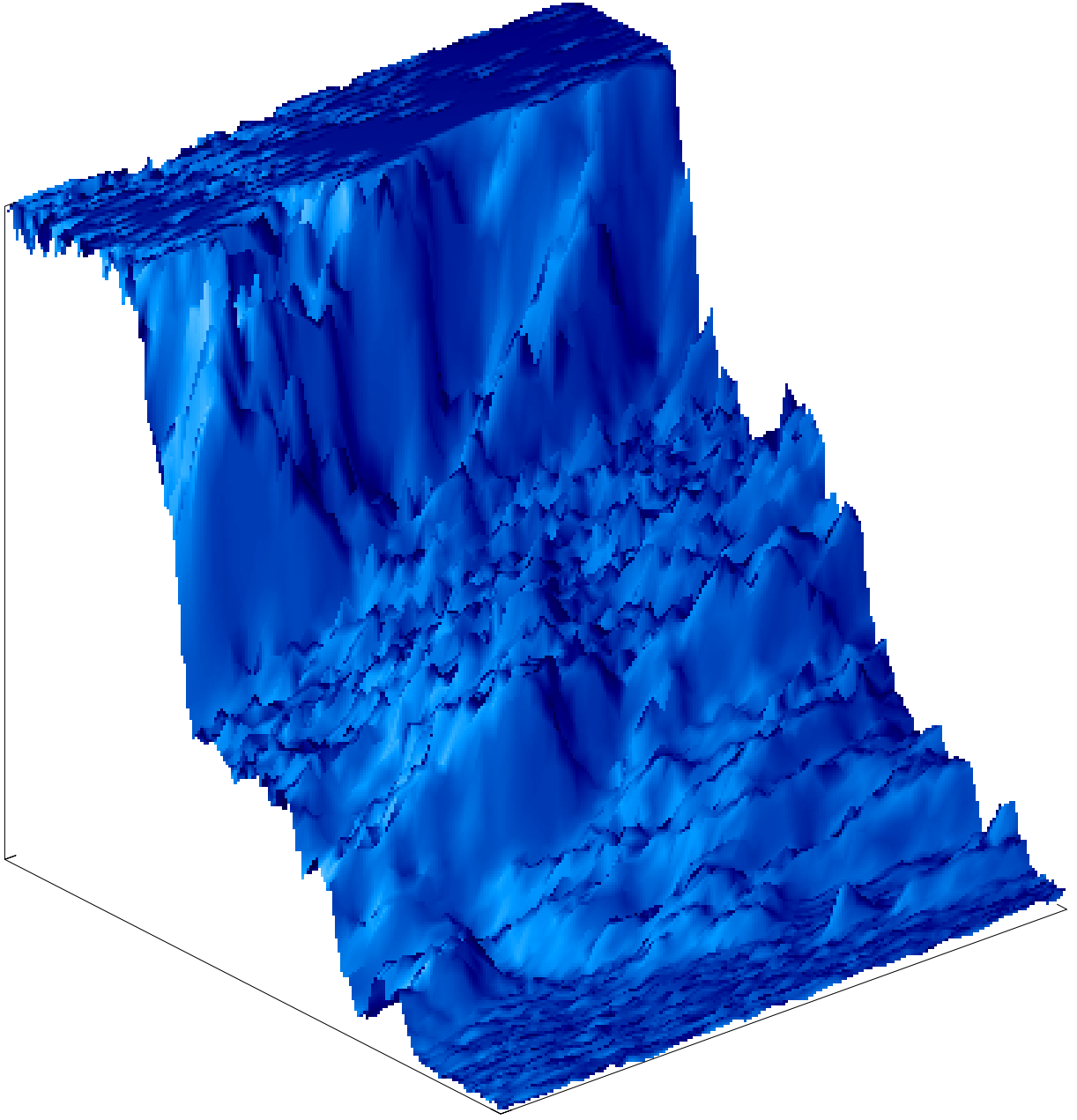


Figure 18: Surface rendering of the two-dimensional spatial refractive index field for the middle vertical third of the image in the bottom left of figure 15, at a spatial resolution of 50×200 pixels. This surface shows the coarse-grained variations of the refractive index across the transverse instantaneous extent of the shear layer encountered by the laser wavefronts.

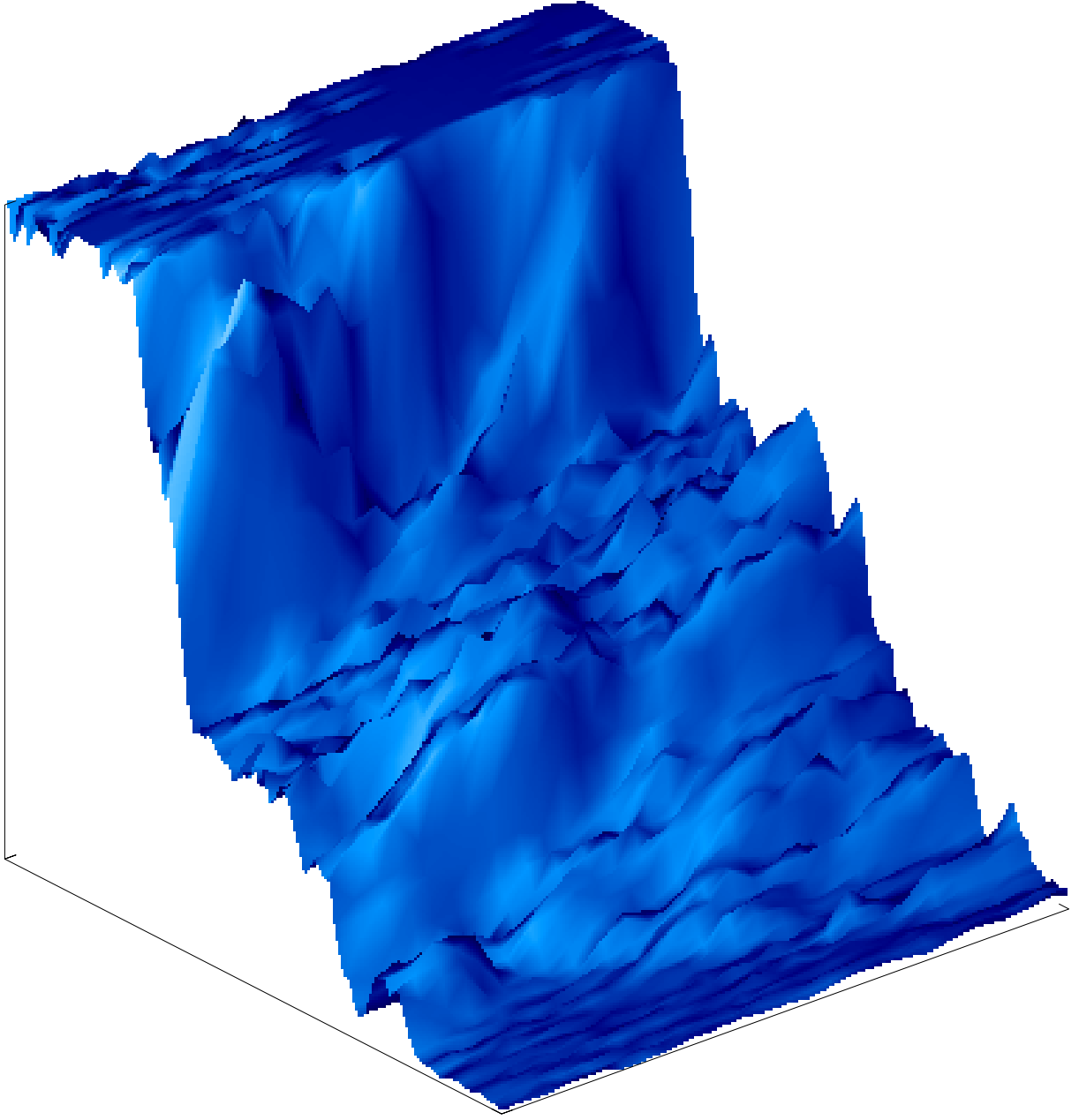


Figure 19: Surface rendering of the two-dimensional spatial refractive index field for the middle vertical third of the image in the bottom right of figure 15, at a spatial resolution of 25×100 pixels. This surface shows the coarse-grained variations of the refractive index across the transverse instantaneous extent of the shear layer encountered by the laser wavefronts.

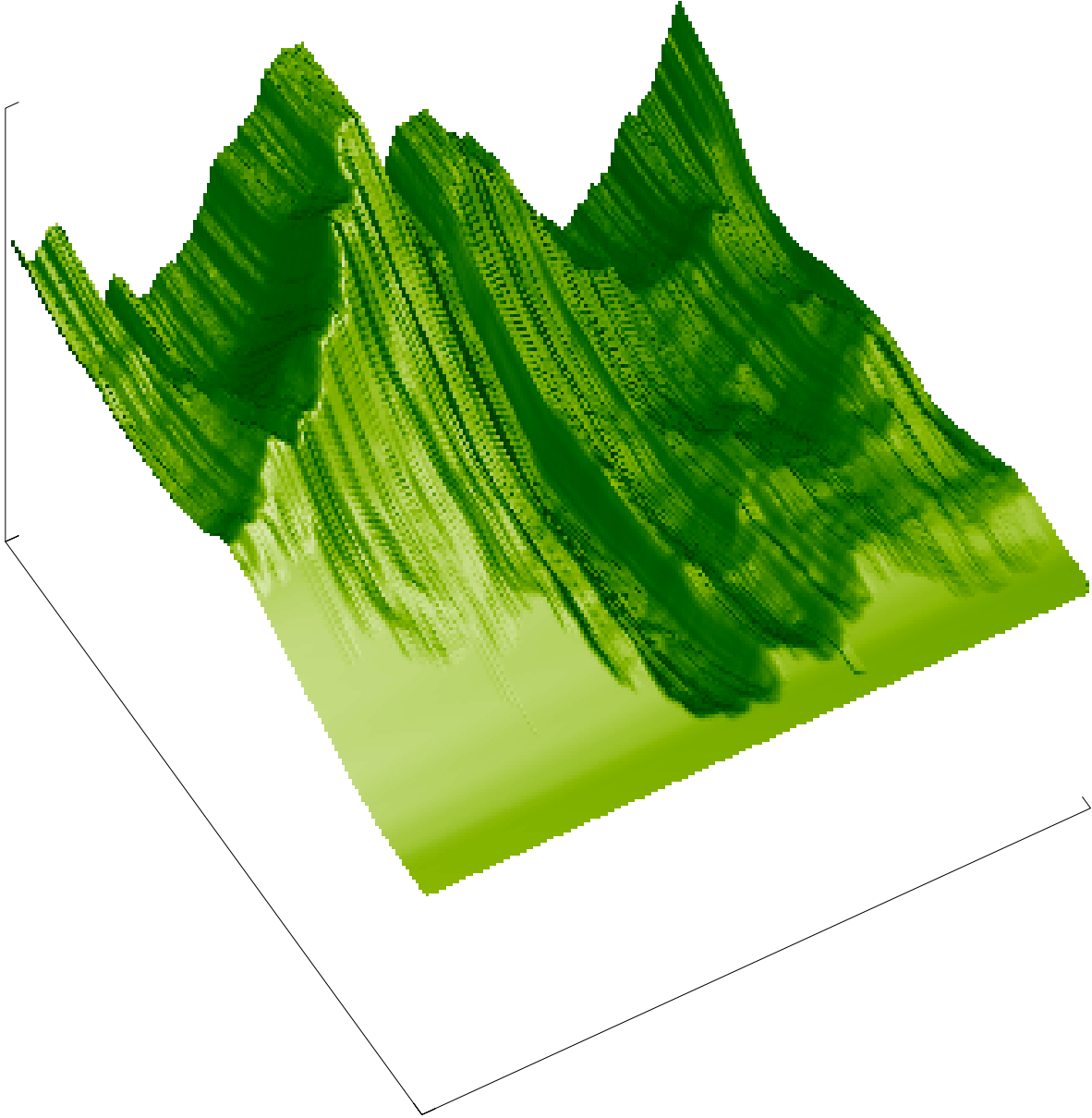


Figure 20: Surface rendering of the cumulative optical path difference variations for laser wavefront propagation through the refractive index field of figure 16 across the transverse extent of the shear layer. This surface rendering is for the full spatial resolution of $\sim 1000 \times 1000$ pixels.

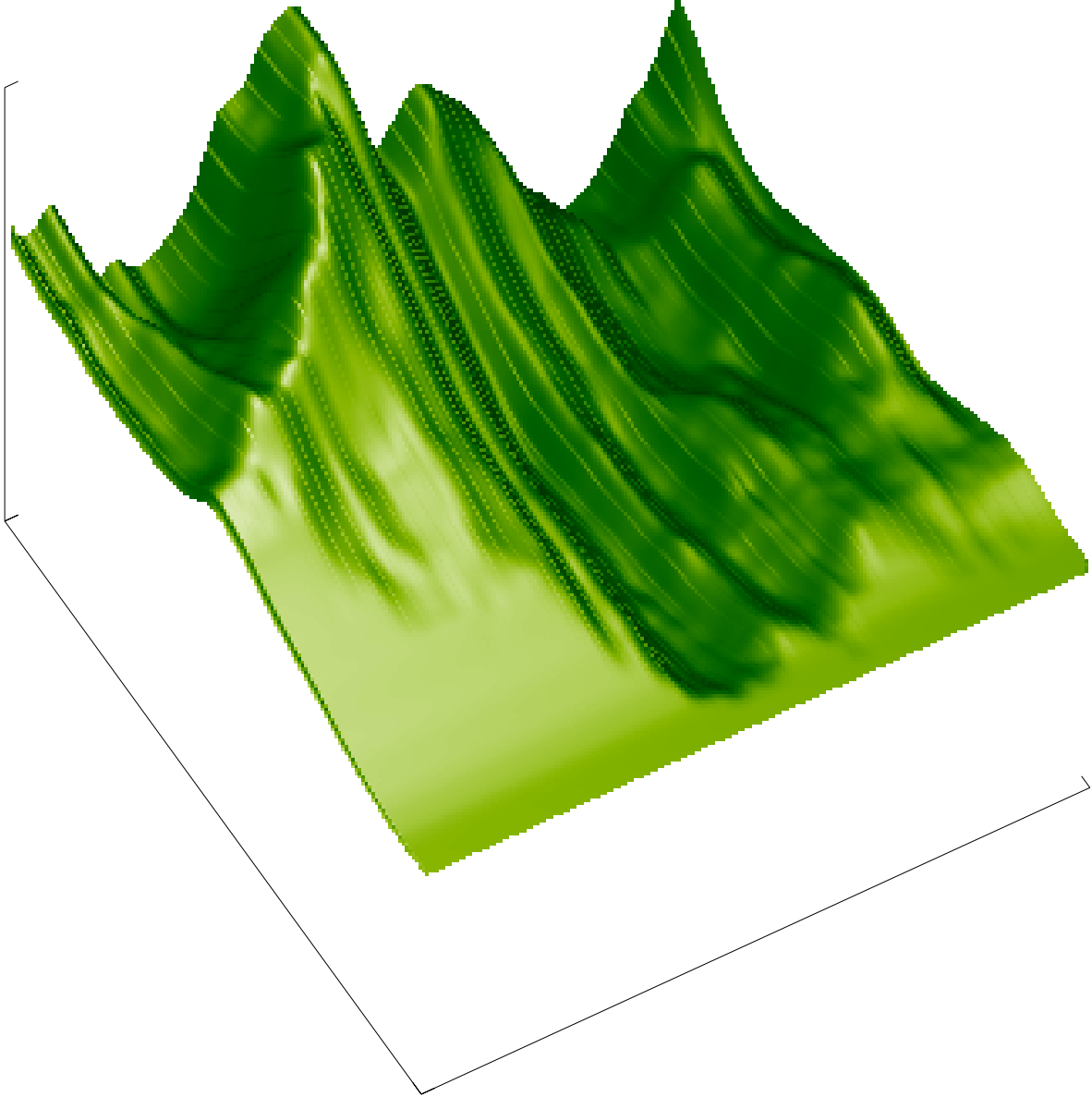


Figure 21: Surface rendering of the cumulative optical path difference variations for laser wavefront propagation through the coarse-grained refractive index field of figure 17 across the transverse extent of the shear layer. This surface rendering is for the reduced spatial resolution of $\sim 75 \times 75$ pixels.

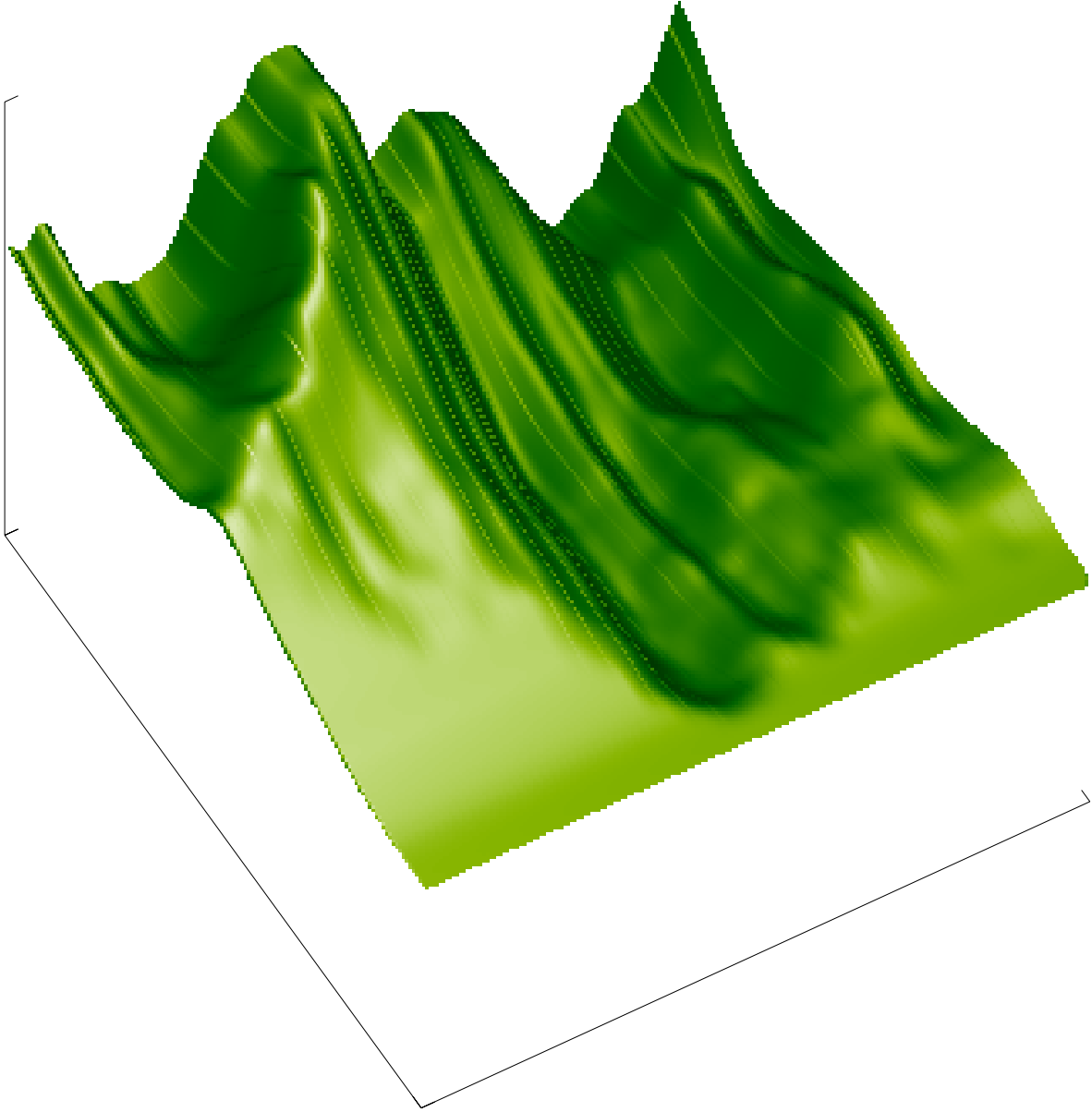


Figure 22: Surface rendering of the cumulative optical path difference variations for laser wavefront propagation through the coarse-grained refractive index field of figure 18 across the transverse extent of the shear layer. This surface rendering is for the reduced spatial resolution of $\sim 50 \times 50$ pixels.

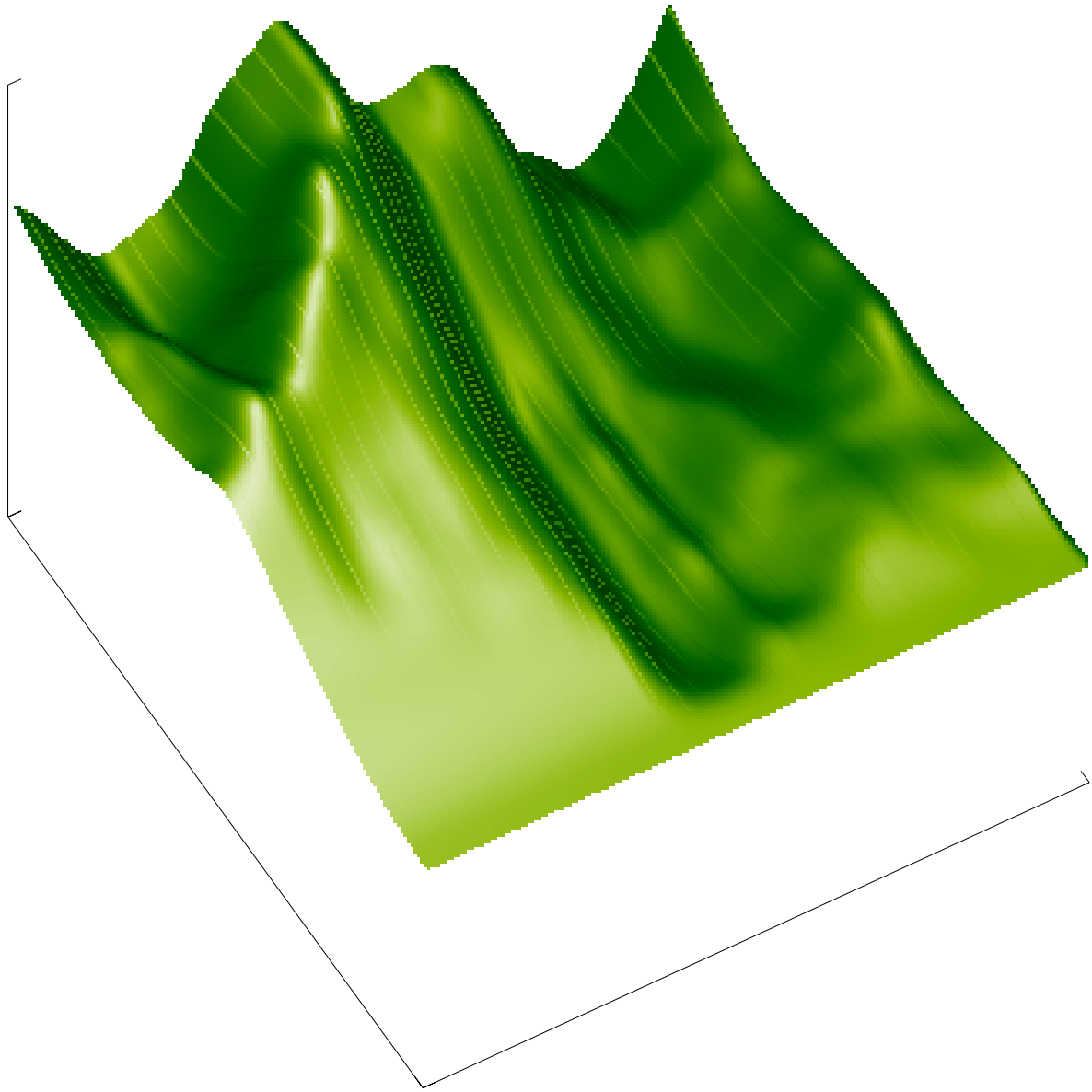


Figure 23: Surface rendering of the cumulative optical path difference variations for laser wavefront propagation through the coarse-grained refractive index field of figure 19 across the transverse extent of the shear layer. This surface rendering is for the reduced spatial resolution of $\sim 30 \times 30$ pixels.

Multiresolution results for both the refractive-index behavior and the aero-optical cumulative interactions are shown in the sequences in figure 15 and figures 16 through 19. The first sequence, in figures 15, shows the coarse-graining in refractive field information as the resolution is reduced. The second sequence, in figures 16 through 19, shows visualizations of the variations in the mixing signature of the refractive index across the shear layer. The third sequence, in figures 20 through 23, shows the multiresolution effects on the cumulative aero-optical interactions. It is directly evident, in these three sequences, that the primary structure of the aero-optical wavefront aberrations along the beam propagation paths is highly robust to the coarse-graining or resolution reduction. This is a key finding with implications both experimentally and computationally, vis-à-vis bandwidth requirements for experimental flow/beam control and resolution requirements for computational simulations respectively, regarding the aero-optical interactions for directed-energy research as well as development.

3. Conclusions and Implications

In the research reported in this grant period, a key focus is the role of refractive interfaces in large scale aero-optical interactions in high Reynolds number compressible separated shear layers. Direct imaging of the refractive index field and interfaces is conducted using laser induced fluorescence of acetone vapor molecularly premixed in air and digital photography techniques. High resolution two-dimensional spatial images of the refractive index field have been recorded. The Reynolds number based on the large scale visual thickness is $Re \sim 6 \times 10^6$, the convective Mach number is $M_c \sim 0.4$, and the test section pressure is $p \sim 3 \text{ atm}$. The refractive index fields have been examined to identify the dominant interfacial contributions to the propagation and distortion of optical wavefronts. Highly irregular networks of spatially-isolated high gradient interfaces are evident both in the flow interior and at the outer boundaries. These high gradient interfaces are found to be primarily responsible for the large scale aero-optical interactions. Specifically, a physical model utilizing these high gradient boundaries is able to reproduce well the large scale optical wavefront distortions. Significant robustness is found for the optical distortions in terms of reduction in the refractive field information by retaining high refractive gradient interfaces. This has implications for optimization studies in aero-optics because it suggests that effective modification of the optical aberrations may be sought in terms of altering the structure of the high gradient interfaces.

The multiresolution study based on the combined experimental/computational approach provides support for ongoing studies of aero-optical interactions in laser beam propagation through highly-separated turbulent flows. The robustness to resolution reduction, i.e. coarse-graining, is an encouraging finding from an applications point of view, e.g. in terms of large-scale flow organization and disorganization [61, 14]. The large Reynolds number flow conditions are achieved with a specially-designed experimental laboratory facility. This variable-pressure flow facility enables direct imaging of the turbulent refractive-index field at Reynolds numbers of $Re \sim 10^6$ in controlled laboratory flows. These large Reynolds numbers are necessary in order to exceed, in this case by two orders of magnitude, the minimum value of $Re \sim 10^4$ representative of fully-developed turbulence. Laser-induced fluorescence in purely-gaseous flows, using acetone

vapor seeded in air, is utilized to directly image the turbulent refractive-index spatial fluctuations along the beam propagation paths with a high-resolution intensified CCD camera. Direct imaging of the refractive-index fields is enabled by propagating pulsed ultraviolet laser sheets through the highly-separated shear layers. The present methodology provides a means to study the laser beam wavefronts along the entire propagation path in large Reynolds number flows, which are otherwise inaccessible for purely-computational studies that would be limited to lower Reynolds numbers or small-scale turbulence modeling. The present multiresolution study enables an examination of the sensitivity of the aero-optical aberrations with regard to the structure of the refractive interfaces encountered along the propagation path. The evidence of robustness of the aero-optical aberrations to the amount of reduction in refractive field information, over a wide range, provides a key ingredient for experimental and computational advances in aero-optical aspects of directed-energy research and development.

References

- [1] E. J. Jumper and E. J. Fitzgerald. Recent advances in aero-optics. *Prog. Aerospace Sci.*, 37:299–339, 2001.
- [2] H. J. Catrakis. Turbulence and the dynamics of fluid interfaces with applications to mixing and aero-optics. In N. Ashgriz and R. Anthony, editors, *Recent Research Developments in Fluid Dynamics Vol. 5*, pages 115–158. Transworld Research Network Publishers, ISBN 81-7895-146-0, Kerala, India, 2004.
- [3] H. W. Liepmann. Deflection and diffusion of a light ray passing through a boundary layer. Douglas Aircraft Company Report SM-14397, Santa Monica, CA, May 1952.
- [4] H. A. Stine and W. Winovich. Light diffusion through high-speed turbulent boundary layers. NACA Research Memorandum A56B21, 1956.
- [5] D. Kyraizis. Optical degradation by turbulent free shear layers. In S. S. Cha and J. D. Trolinger, editors, *Optical Diagnostics in Fluid and Thermal Flow*, pages 170–181, Orlando, Florida, 1993. SPIE.
- [6] P. E. Dimotakis, H. J. Catrakis, and D. C. L. Fourquette. Flow structure and optical beam propagation in high-Reynolds-number gas-phase shear layers and jets. *J. Fluid Mech.*, 433:105–134, 2001.
- [7] M. Jones and E. E. Bender. CFD-based computer simulation of optical turbulence through aircraft flowfields and wakes. In *AIAA 32nd Plasmadynamics and Lasers Conference, AIAA 2001-2798*, Anaheim, CA, June 2001.
- [8] E. Tromeur, E. Garnier, P. Sagaut, and C. Basdevant. Large eddy simulations of aero-optical effects in a turbulent boundary layer. *J. Turbulence*, 4(5):1–22, 2003.
- [9] E. J. Fitzgerald and E. J. Jumper. The optical distortion mechanism in a nearly incompressible free shear layer. *J. Fluid Mech.*, 512:153–189, 2004.

- [10] H. J. Catrakis and R. C. Aguirre. New interfacial fluid thickness approach in aer-optics with applications to compressible turbulence. *AIAA J.*, 42(10):1973–1981, 2004.
- [11] R. J. Hill. Review of optical scintillation methods of measuring the refractive-index spectrum, inner-scale, and surface fluxes. *Waves in Random Media*, 2:179–201, 1992.
- [12] N. T. Clemens. Flow imaging. In *Encyclopedia of Imaging Science and Technology*, pages 390–419. Wiley, 2002.
- [13] R. C. Aguirre and H. J. Catrakis. Aero-optical wavefronts and scale-local characterization in large-Reynolds-number compressible turbulence. *AIAA J.*, 42(10):1982–1990, 2004.
- [14] M. Stanek, N. Sinha, J. Seiner, B. Pearce, and M. Jones. High frequency flow control: suppression of aero-optics in tactical directed energy beam propagation and the birth of a new model (part I). In *AIAA 33rd Plasmadynamics and Lasers Conference, AIAA 2002-2272*, Maui, HI, June 2002.
- [15] K. R. Sreenivasan. Fractals and multifractals in fluid turbulence. *Annu. Rev. Fluid. Mech.*, 23:539–600, 1991.
- [16] H. J. Catrakis, R. C. Aguirre, J. Ruiz-Plancarte, R. D. Thayne, B. A. McDonald, and J. W. Hearn. Large-scale dynamics in turbulent mixing and the three-dimensional space-time behaviour of outer fluid interfaces. *J. Fluid Mech.*, 471:381–408, 2002.
- [17] H. J. Catrakis, R. C. Aguirre, and J. Ruiz-Plancarte. Area–volume properties of fluid interfaces in turbulence: scale-local self-similarity and cumulative scale dependence. *J. Fluid Mech.*, 462:245–254, 2002.
- [18] R. C. Aguirre and H. J. Catrakis. On intermittency and the physical thickness of turbulent fluid interfaces. *J. Fluid Mech.*, 540:39–48, 2005.
- [19] P. Moin and K. Mahesh. Direct numerical simulations: A tool in turbulence research. *Annu. Rev. Fluid. Mech.*, 30:539–578, 1998.
- [20] C. Meneveau and J. Katz. Scale-invariance and turbulence models for large-eddy simulation. *Annu. Rev. Fluid. Mech.*, 32:1–32, 2000.
- [21] C. R. Truman and M. J. Lee. Effects of organized turbulence structures on the phase distortion in a coherent optical beam propagating through a turbulent shear flow. *Phys. Fluids A*, 2:851–857, 1990.
- [22] H. G. E. Hentschel and I. Procaccia. Passive scalar fluctuations in intermittent turbulence with applications to wave propagation. *Phys. Rev. A.*, 28:417–426, 1983.
- [23] C. Schwartz, G. Baum, and E. N. Ribak. Turbulence-degraded wave fronts as fractal surfaces. *J. Opt. Soc. Am.*, 11(1):444–451, 1994.
- [24] G. L. Brown and A. Roshko. On density effects and large scale structure in turbulent mixing layers. *J. Fluid Mech.*, 64:775–816, 1974.

- [25] S. Morris and J. Foss. Measurements of velocity-vorticity correlations in a shear layer and boundary layer at high Reynolds number. In *3rd International Symposium on Turbulence and Shear Flow Phenomena, TSFP3-224*, Sendai, Japan, 2003.
- [26] A. Roshko. The mixing transition in free shear flows. In J. Jiménez, editor, *The Global Geometry of Turbulence*, pages 3–11. Plenum, 1991.
- [27] N. T. Clemens and M. G. Mungal. Large-scale structure and entrainment in the supersonic mixing layer. *J. Fluid Mech.*, 284:171–216, 1995.
- [28] M. Sirieix and J. L. Solignac. Contribution a l’etude experimentale de la couche de melange turbulent isobare d’un ecoulement supersonique. Separated Flows, AGARD CP4, 1966.
- [29] H. Ikawa and T. Kubota. Investigation of supersonic turbulent mixing layer with zero pressure gradient. *AIAA J.*, 31:2247–2254, 1975.
- [30] N. Chinzei, G. Masua, T. Komuro, A. Murakami, and K. Kudou. Spreading of two-stream supersonic turbulent mixing layers. *Phys. Fluids*, 29:1345–1347, 1986.
- [31] D. Papamoschou and A. Roshko. The compressible turbulent shear layer: an experimental study. *J. Fluid Mech.*, 197:453–477, 1988.
- [32] M. Samimy and G. S. Elliot. Effects of compressibility on the characteristics of free shear layers. *AIAA J.*, 28:439–445, 1990.
- [33] S. G. Goebel and J. C. Dutton. Experimental study of compressible turbulent mixing layers. *AIAA J.*, 29:538–546, 1991.
- [34] J. L. Hall, P. E. Dimotakis, and H. Rosemann. Experiments in non-reacting compressible shear layers. *AIAA J.*, 31(2247-2254), 1993.
- [35] S. Barre, C. Quine, and J. P. Dussauge. Compressibility effects on the structure of mixing layers: experimental results. *J. Fluid Mech.*, 259:47–78, 1994.
- [36] M. D. Slessor, M. Zhuang, and P. E. Dimotakis. Turbulent shear-layer mixing: growth-rate compressibility scaling. *J. Fluid Mech.*, 414:35–45, 2000.
- [37] T. Rossmann, M. G. Mungal, and R. K. Hanson. Evolution and growth of large-scale structures in high compressibility mixing layers. *J. Turbulence*, 3(009):1–19, 2002.
- [38] A. Lozano, B. Yip, and R. K. Hanson. Acetone: a tracer for concentration measurements in gaseous flows by planar laser-induced fluorescence. *Exps. Fluids*, 13:369–376, 1992.
- [39] M. C. Thurber and R. K. Hanson. Pressure and composition dependences of acetone laser-induced fluorescence with excitation at 248, 266, and 308 nm. *Appl. Phys. B*, 69:229–240, 1999.
- [40] M. Smith, A. Smits, and R. Miles. Compressible boundary-layer density cross sections by UV Rayleigh scattering. *Opt. Lett.*, 14:916–918, 1989.

- [41] A. J. Smits and T. T. Lim. *Flow Visualization Techniques and Examples*. Imperial College Press, London, UK, 2000.
- [42] M. M. Koochesfahani and P. E. Dimotakis. Laser-induced fluorescence measurements of mixed fluid concentration in a liquid plane shear layer. *AIAA J.*, 23:1700–1707, 1985.
- [43] J. C. LaRue and P. A. Libby. Temperature and intermittency in the turbulent wake of a heated cylinder. *Phys. Fluids*, 17:873–878, 1975.
- [44] D. K. Bisset, J. C. Hunt, and M. M. Rogers. The turbulent/non-turbulent interface bounding a far wake. *J. Fluid Mech.*, 451:381–410, 2002.
- [45] D. D. Joseph and L. Preziosi. Heat waves. *Rev. Mod. Phys.*, 61:41–73, 1989.
- [46] E. Villiermaux and C. Innocenti. On the geometry of turbulent mixing. *J. Fluid Mech.*, 393:123–147, 1999.
- [47] R. C. Aguirre and H. J. Catrakis. Scalar-threshold dependence and internal dynamics in turbulent jets. *Phys. Fluids*, 17(038103), 2004.
- [48] K. R. Sreenivasan. On the fine-scale intermittency of turbulence. *J. Fluid Mech.*, 151:81–103, 1985.
- [49] L. K. Su and N. T. Clemens. Planar measurements of the full three-dimensional scalar dissipation rate in gas-phase turbulent flows. *Exps. Fluids*, 27:507–521, 1999.
- [50] W. J. A. Dahm and K. B. Southerland. Experimental assessment of Taylor’s hypothesis and its applicability to dissipation estimates in turbulent flows. *Phys. Fluids*, 9(7):2101–2107, 1997.
- [51] A. Mani, M. Wang, and P. Moin. Computation of optical beam propagation through numerically simulated turbulence. *Bull. Am. Phys. Soc.*, 2003.
- [52] S. E. Elghobashi and A. T. Wassel. The effect of turbulent heat transfer on the propagation of an optical beam across supersonic boundary/shear layers. *Intl J. Heat Mass Transfer*, 23:1229–1241, 1980.
- [53] R. Z. Yahel. Turbulence effects on high energy laser beam propagation in the atmosphere. *Appl. Opt.*, 29:3088–3095, 1990.
- [54] H. W. Liepmann. Aspects of the turbulence problem. Part 1: I. Introduction, II. Stationary stochastic processes, III. Turbulence effects upon linear systems. *Z. angew. Math. Phys.*, 3:321–342, 1952.
- [55] M. Born and E. Wolf. *Principles of optics: electromagnetic theory of propagation, interference and diffraction of light*. Cambridge Univ. Press, seventh edition, 1999.
- [56] K. G. Gilbert and L. J. Otten. Aero-optical phenomena. In *Progress in Astronautics and Aeronautics*, volume 80. American Institute of Aeronautics and Astronautics, 1982.

- [57] G. W. Sutton. Aero-optical foundations and applications. *AIAA J.*, 23(10):1525–1537, 1985.
- [58] L. C. Andrews and R. L. Phillips. *Laser beam propagation through random media*. SPIE Optical Engineering Press, Bellingham, WA, 1998.
- [59] G. W. Sutton. Effects of turbulent fluctuations in an optically active fluid medium. *AIAA J.*, 7:1737–1743, 1969.
- [60] Y.-P. Tsai and W. H. Christiansen. Two-dimensional numerical simulation of shear layer optics. *AIAA J.*, 28:2092, 1990.
- [61] J. P. Siegenthaler, E. J. Jumper, and A. Asghar. A preliminary study in regularizing the coherent structures in a planar, weakly-compressible, free shear layer. In *AIAA 41st Aerospace Sciences Meeting & Exhibit, AIAA 2003-0680*, Reno, NV, January 2003.